The Astrophysical Journal, 926:25 (17pp), 2022 February 10 https://doi.org/10.3847/1538-4357/ac41c3

Sh 2-301: A Blistered H II Region Undergoing Star Formation

Rakesh Pandey[1,2], Saurabh Sharma[1], Lokesh K. Dewangan[3], Devendra K. Ojha[4], Neelam Panwar[1], Swagat Das[5], D. P. Bisen[2], Arpan Ghosh[1,2], and Tirthendu Sinha[1]

[1] Aryabhatta Research Institute of Observational Sciences (ARIES), Manora Peak, Nainital, 263 002, India; pandey.rakesh405@gmail.com
[2] School of Studies in Physics and Astrophysics, Pt. Ravishankar Shukla University, Raipur, (C.G.), 492 010, India
[3] Physical Research Laboratory, Navrangpura, Ahmedabad, 380 009, India
[4] Tata Institute of Fundamental Research (TIFR), Homi Bhabha Road, Colaba, Mumbai, 400 005, India
[5] Indian Institute of Science Education and Research(IISER), Tirupati, 517 507, India

Received 2021 August 30; revised 2021 November 17; accepted 2021 November 29; published 2022 February 9

Abstract

We present a multiwavelength study of the H II region Sh 2-301 (S301) using deep optical data, near-infrared data, radio continuum data, and other archival data at longer wavelengths. A cluster of young stellar objects (YSOs) is identified in the northeast (NE) direction of S301. The Hα and radio continuum images trace the distribution of the ionized gas surrounding a massive star, ALS 207, and the S301 H II region is bounded by an arc-like structure of gas and dust emission in the southeastern direction. The northwestern part of S301 seems to be devoid of gas and dust emission, while the presence of molecular material between the NE cluster and the central massive star ALS 207 is found. The distribution of warm dust emission, ionized gas, and neutral hydrogen together suggests a blistered morphology of the S301 H II region powered by ALS 207, which appears to be located near the edge of the cloud. The location of the NE cluster embedded in the cold molecular cloud is found opposite to the blistered morphology. There is a noticeable age difference investigated between the massive star and the NE cluster. This age difference, pressure calculation, photodissociation regions, and the distribution of YSOs favor the positive feedback of the massive star ALS 207 in S301. On a wider scale of S301, the H II region and the young stellar cluster are depicted toward the central region of a hub-filamentary system, which is evident in the infrared images.

Unified Astronomy Thesaurus concepts: Interstellar dust extinction (837); Interstellar filaments (842); Stellar-interstellar interactions (1576); Star formation (1569)

Supporting material: machine-readable tables

1. Introduction

Previous studies of bubbles associated with H II regions have suggested that their expansion probably triggers 14%–30% of the star formation in our Galaxy (e.g., Deharveng et al. 2010; Kendrew et al. 2012; Thompson et al. 2012). Feedback from massive stars ionizes the surrounding molecular cloud through their immense UV radiation and powerful winds, resulting in an H II region, a glowing nebula of ionized gas. Lopez et al. (2014) have discussed the various feedback processes in detail. Feedback from a massive star may inhibit or terminate further star formation in the immediate vicinity (termed as "negative feedback") or it can also promote and accelerate the star formation (known as "positive feedback"). Out of these two outcomes which one will dominate depends not only on the process itself but also on the properties of the clouds (Shima et al. 2017). Stars born out of these processes are generally assembled in a group or cluster, an entity having a collection of physically related stars. The physical features such as shape, size, age, and mass distribution of these clusters vary with their host environment and seem to show the imprints of star formation processes themselves (Lada & Lada 2003; Allen et al. 2007; Grasha et al. 2017, 2018). Therefore, stellar clusters constitute the nearest laboratories for direct astronomical investigation of the physical processes of star formation and early evolution. The first generation of massive stars in these regions also play a very important role as they can give very crucial clues on the star formation through entirely different physical processes. Thus, we can have a mix of stars in the same star-forming region, giving hints of their origin. Dale et al. (2015) have discussed other star formation processes like cloud–cloud collision, filamentary interactions, etc. In recent years, many authors have pointed out the active role of filamentary structures and their subsequent interaction in star formation (Schneider et al. 2012; Dewangan et al. 2017b, 2020a). Filamentary structures are often seen harboring young stellar clusters and massive star-forming clumps, yet their precise role in star formation is not very well understood.

With an aim to investigate the stellar clustering and their origin, star formation, shape of the mass function (MF), and effects of the feedback from massive stars on these processes, we have performed a multiwavelength study of the H II region "Sh 2-301" (hereafter, S301). This is a southern sky ($\alpha_{2000} = 07^h09^m55^s$, $\delta_{2000} = -18°29'36''$) Galactic H II region located in a very large molecular cloud complex ($\sim 6° \times 3°$; Russeil et al. 1995). Avedisova & Palous (1989) placed this region in a star-forming region, "SFR 231.44-4.41", along with the reflection nebulae Bran 6 and Bran 7. This region is thought to be ionized by a massive O-type star, ALS 207, and also harbors two B-type stars, ALS 208 and ALS 212 (Moffat et al. 1979; Garmany et al. 2015; Maíz Apellániz et al. 2016). Despite showing very interesting features at different wavelengths, this region is one of the most poorly studied H II regions in our Galaxy. In Figure 1, we show a color-composite image made by using 3.4 μm (red), *K*-band (green), and Hα (blue) images. The image clearly shows a heated environment in the central region near the massive star

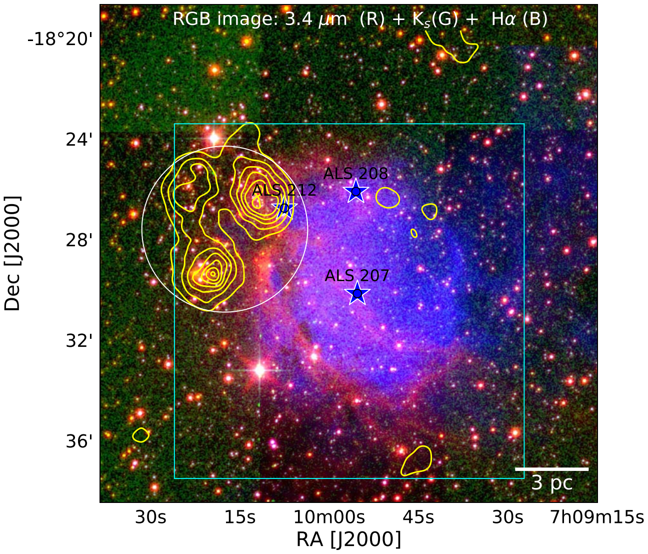

Figure 1. Color-composite image of the ∼18$'$.5 × 18$'$.5 field of view (FOV) around the S301 H II region obtained using the Wide-field Infrared Survey Explorer 3.4 μm (red), K-band (green) and UK Schmidt Telescope (UKST) Hα (blue). The locations of three massive stars, ALS 207, ALS 208 and ALS 212, are also shown in the figure by star symbols (Moffat et al. 1979). The white circle represents the extent of the clustering identified in the present analysis (see Section 3.2). The stellar surface density of the near-infrared (NIR) sources generated using the nearest-neighbor method (see Section 3.2) is shown with yellow contours. The lowest contour is 1σ above the mean value (i.e., 2.6 stars arcmin^{-2}), where the step size is $1\sigma = 2$ stars arcmin^{-2}. The cyan box represents the FOV covered in the NIR (TIRSPEC) observation.

ALS 207, as indicated by the Hα emission. The heated region is surrounded by gas and dust indicated by the infrared (IR) emissions. All these morphologies suggest a prominent feedback from the massive star which is influencing its surroundings. Thus, S301 is an ideal site for our investigation of the feedback of a massive star in the region.

We organize this work as follows. In Section 2, we describe the optical/IR observations and data reduction along with the archival data sets used in our analysis. In Section 3, we describe the schemes used to study the stellar densities, membership probability, distance, reddening, age, MF, identification of young stellar objects (YSOs), etc. The main results of the present study are summarized and discussed in Section 4 and we conclude in Section 5.

2. Observation and Data Reduction

2.1. Imaging Data

We have observed the S301 region in broadband optical ($UBV(RI)_c$) filters using the 1.3 m Devasthal Fast Optical Telescope (DFOT) of the Aryabhatta Research Institute of Observational Sciences, Nainital, India. The imaging camera on the telescope is a 2K × 2K CCD covering a ∼18$'$.5 × 18$'$.5 field of view (FOV) of the sky. The readout noise and gain of the CCD are 8.29 e^- and 2.2 e^-/ADU, respectively. Images of the target field (S301) and standard field (SA98) (α_{J2000}: 06$^{\rm h}$52$^{\rm m}$14$^{\rm s}$, δ_{J2000}: $-00°18'59''$; Landolt 1992), along with flat and bias frames were taken during the observations. We have also observed S301 in broadband near-IR (NIR; JHK) filters using the TIFR Near Infrared Spectrometer and Imager (TIRSPEC)[6] mounted on the 2 m Himalayan Chandra Telescope (HCT), Hanle, Ladakh, India. The specifications of the instrument and the detector array are mentioned in Ninan et al. (2014). The FOV of the instrument is $307'' \times 307''$ in the imaging mode. We took nine pointings covering a $15' \times 15'$ FOV around the central massive star (ALS 207). Five dithered positions with 7 frames of 20 s in each position were used to create average combined images in the J, H, and K filters. The complete log of observation is provided in the Table 1. For image cleaning, photometry, and astrometry, we used standard data-reduction procedures, as mentioned in Pandey et al. (2020b).

We have followed the procedures outlined by Stetson (1992) for calibration of the optical instrumental magnitudes to the standard magnitudes (Vega) by using the following calibration equations:

$$u = U + (5.328 \pm 0.021) - (0.046 \pm 0.01)(U - B) + (0.490 \pm 0.061)X_U, \quad (1)$$

$$b = B + (3.292 \pm 0.007) - (0.127 \pm 0.006)(B - V) + (0.208 \pm 0.006)X_B, \quad (2)$$

$$v = V + (2.488 \pm 0.007) + (0.072 \pm 0.005)(V - I_c) + (0.131 \pm 0.009)X_V, \quad (3)$$

$$r_c = R_c + (1.797 \pm 0.006) + (0.102 \pm 0.010)(V - R_c) + (0.074 \pm 0.007)X_R, \quad (4)$$

$$i_c = I_c + (2.529 \pm 0.009) - (0.013 \pm 0.006)(V - I_c) + (0.011 \pm 0.007)X_I, \quad (5)$$

where U, B, V, R_c, I_c, and u, b, v, r_c, i_c are the standard and instrumental magnitudes of the standard stars in the SA98 field, respectively. Instrumental magnitudes were normalized for the exposure time and X is the air mass at the time of observation.

The instrumental magnitudes in the NIR bands were transferred to the standard magnitudes (Vega) by using the following transformation equations:

$$(J - K) = (0.99 \pm 0.02) \times (j - k) + (0.61 \pm 0.01), \quad (6)$$

$$(H - K) = (0.94 \pm 0.04) \times (h - k) + (0.66 \pm 0.01), \quad (7)$$

$$(K - k) = (-0.12 \pm 0.05) \times (H - K) + (-4.95 \pm 0.01), \quad (8)$$

where JHK and jhk are the standard and instrumental magnitudes of the common stars from the Two Micron All Sky Survey (2MASS) catalog and HCT observations, respectively. The coefficients for the above equations were generated separately for each pointing.

We have compared our derived standard magnitudes with the available V- and B-band standard magnitudes in the "AAVSO Photometric All-Sky Survey" (APASS)[7] archive, and the photometric agreement is found to be reasonable.

Finally, we made a photometric catalog by taking only those stars which have photometric errors <0.1 mag. The photometry of the stars that were saturated in our deep observations was taken from the short exposures and 2MASS catalog for the optical and NIR bands, respectively. The number of sources detected in different bands and their detection limits are given in Table 2.

---

[6] http://www.tifr.res.in/~daa/tirspec/

[7] The AAVSO Photometric All-Sky Survey (APASS), https://www.aavso.org/apass.

Table 1
Log of Observations

Telescope/Instrument (Date of Observations)	Comments (Filter)	Exp. (sec) × No. of Frames
1.3 m DFOT/2K CCD	Optical imaging of S301	
[2019 Dec 25]	U	300 × 3
″	B	300 × 3
″	V	180 × 3, 60 × 3
″	R_c	180 × 3, 60 × 3, 10 × 3
″	I_c	180 × 3, 60 × 3, 10 × 3
[2018 Jan 16]	I_c	1200 × 5
[2018 Jan 16]	V	1800 × 5
	Optical imaging of Standard field (SA98)	
[2019 Dec 25]	U	300 × 4
″	B	300 × 1, 120 × 4, 60 × 1
″	V	60 × 6, 30 × 6
″	R_c	30 × 6, 20 × 6
″	I_c	30 × 3, 20 × 4
2 m HCT/TIRSPEC	NIR imaging of S301 (Nine pointings)	
[2018 Dec 25 & 2018 Dec 26]	J	20 × 35
″	H	20 × 35
″	K	20 × 35
2 m HCT	Optical spectroscopy of ALS 207, ALS 208, and ALS 212	
[2019 Aug 20]	GRISM 7	600 × 1, 900 × 1, 900 × 1

2.1.1. Completeness of the Photometric Data

Due to nebulosity, crowding of the stars, detection limits, etc., the photometric data may be incomplete. It is thus very important to know the completeness limit in terms of mass for MF analyses. We have used the procedure outlined in Sharma et al. (2008) to determine the completeness factor. In this method we artificially added stars of known magnitudes and position in the original images using the IRAF routine ADDSTAR. After gaining images with artificially added stars, we performed photometry of those images as we did for the original images (keeping all the parameters the same). Finally, the completeness factor can be easily determined by taking the ratio of the number of stars recovered to the added stars, in different magnitude bins as a function of magnitude. In Figure 2, we show the completeness factor in different bands as a function of magnitude. As expected, the completeness of the data decreases with fainter magnitudes. The completeness limits in terms of magnitudes and masses in different bands are given in Table 2.

Table 2
Completeness of the Photometric Data

Band	Number of Sources[a]	Detection Limit (mag)	Completeness Limit[d] (upto 80 %)	
			(mag)	Mass ($M_\odot$)
U	596	19.5	⋯	⋯
B	1156	20.2	⋯	⋯
V	5236	22.7	21.0	0.4
R[c]	2965	20.7	⋯	⋯
I[c]	5624	21.6	20.0	0.3
J	2277[b]+ 1846[c]	18.4	15.3	0.4
H	2811[b]+ 1534[c]	18.1	15.0	0.4
K	2809[b]+ 970[c]	17.8	15.0	0.3

Notes.
[a] : for 18$'$.5 × 18$'$.5 FOV;
[b] : data from TIRSPEC;
[c] : data from 2MASS for the bright stars;
[d] : for distance = 3.54 kpc and $E(B - V) = 0.5$ mag.

2.2. Spectroscopic Data

We performed spectroscopic observations of three bright sources, ALS 207, ALS 208 and ALS 212 (see Figure 1), in the S301 region, using the Hanle Faint Object Spectrograph Camera (HFOSC) instrument mounted on the HCT, Hanle, India. The observations were performed with GRISM 7 (3800–6840 Å) with a resolution of 1200. A spectroscopic standard star was also observed in the same night for flux calibrations. The log of the spectroscopic observation is provided in Table 1.

Spectroscopic data reduction was performed with IRAF packages using standard procedures (Jose et al. 2012). For wavelength calibration, FeAr and FeNe arc lamps were observed during each night. For flux calibration, standard stars such as Feige 34, Feige 110, and HZ 44 were observed. Aperture extraction, identification of lines using lamps, and dispersion correction were undertaken by the APALL, IDENTIFY, and DISPCOR tasks, respectively. STANDARD, SENSFUNC, and CALIBRATE tasks were used for flux calibration. Finally, the spectrum was normalized using the CONTINUUM task in IRAF. The flux-calibrated normalized spectra of the three sources are shown in Figure 3.

2.3. Radio Continuum Data

Radio continuum observation of the S301 region at 1280 MHz was carried out using the Giant Metrewave Radio Telescope (GMRT) facility on 2018 December 22 (Proposal Code: 35_107; P.I.: Rakesh Pandey). We observed the flux calibrators for ∼15 minutes in the beginning and end of the observation sequence. The phase calibrator is observed periodically along with the target source. In each period, we observed the target for ∼30 minutes and the phase calibrator for ∼5 minutes. The data was reduced using the Astronomical Image Processing System (AIPS). We used the Very Large

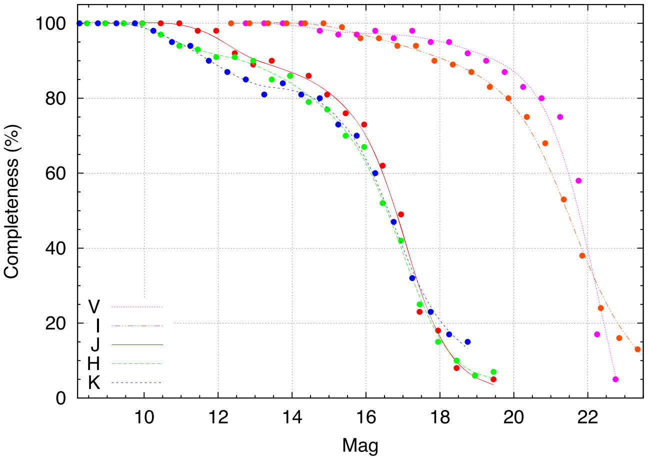

Figure 2. Completeness levels as a function of magnitude in the *V*, *I*, *J*, *H*, and *K* filters derived from the artificial star experiments (ADDSTAR; see Section 2.1.1 for details).

Array (VLA) calibrators 3C147 and 3C286 as flux calibrators and 0744-064 as a phase calibrator. The TVFLG and CALIB tasks were used to remove the bad data points and calibrations, respectively. After getting an image by doing several rounds of self-calibration, primary beam correction was done using the PBCOR task. In this way, we acquired our final reduced image at 1280 MHz with a synthesized beam size of $\sim 7\farcs5 \times 3\farcs4$.

2.4. Archival Data

We used the point-source catalog from the 2MASS in NIR (Cutri et al. 2003) and the Wide-field Infrared Survey Explorer (WISE) (Wright et al. 2010) in mid-IR (MIR) from the the NASA/IPAC Infrared Science Archive (IRSA).[8] We used the recently released Gaia DR3[9] data for the membership determination (Gaia Collaboration et al. 2016, 2018). Apart from that, we also used multiband images from surveys such as Australian Astronomical Observatory/UK Schmidt Telescope (UKST),[10] 2MASS,[11] WISE,[12] AKARI,[13] and Planck[14] (see Pandey et al. 2020b).

To trace the distribution of neutral hydrogen gas toward the S301 region, we also used the H I (21 cm) line data from the HI Parkes All Sky Survey (HIPASS).[15] The angular resolution of the HIPASS data is $15\farcm5$. The channel spacing is 13.2 km s^{-1} and the velocity resolution is 18.0 km s^{-1}.

3. Results and Analysis

3.1. Spectral Analysis of the Bright Stars

The wavelength-calibrated spectra of the bright stars in the S301 region are shown in the Figure 3. To classify the spectral type of these sources, we have used different spectral libraries and criteria available in the literature (e.g., Jacoby et al. 1984; Walborn & Fitzpatrick 1990). In the case of star ALS 207 (shown with the cyan color curve in Figure 3), we can see prominent hydrogen lines (3970, 4101, 4340, 4861, 6563 Å) along with ionized helium lines, i.e., He II (4686, 4542 and 5411 Å) and He I (4144, 4387, 4471, 4713 Å). The line strength of He II usually gets weaker for late O-type stars and is last seen in B0.5-type stars (Walborn & Fitzpatrick 1990). As this line can be seen in the spectrum of ALS 207, we can constrain its spectral type to be earlier than B0.5. The presence of He II lines (4686, 5411 Å) and He II+I (4026 Å) limits the spectral type of ALS 207 to the O type. In the case of ALS 208 and ALS 212 (shown with green and yellow color curves in Figure 3), we can see stronger He I lines at 4026, 4388, and 4417 Å, while the He II 4686 Å line is absent. This implies that the ALS 208 and ALS 212 stars have spectral types later than B0.5. The spectral types of these stars are further constrained by visually comparing their spectra with the spectral library of Jacoby et al. (1984), as shown in the Figure 3 by the red color curves. Thus, ALS 207, ALS 208, and ALS 212 are classified as O6.5 V, B1 III, and B1 V spectral types, respectively. As we have assessed the spectral types of the massive stars based on the low-resolution spectra, we may have an uncertainty of ±1 in the subclass identification. The massive star ALS 207 was previously identified as O6.5 V ((f)) by Maíz Apellániz et al. (2016), which matches with our spectral classification with an additional ((f)) feature in the spectra. The ((f)) feature denotes the weak N III (4634-40-42 Å) emission feature along with the strong He II (4686 Å) absorption feature. These two features are also quite evident in the observed spectra of ALS 207 (Figure 3).

3.2. Search for Stellar Clustering/Grouping in the S301 Region

3.2.1. Isodensity Contours: The Northeast Cluster

As most of the young star clusters are associated with active star-forming regions, we determined stellar surface-density distributions to identify any kind of clustering/groupings present in the S301 region. We performed the nearest-neighbor (NN) method on the 2MASS NIR catalog to generate surface-density maps in the $\sim 18\farcm5 \times 18\farcm5$ FOV around the S301 H II region. In a $20'' \times 20''$ grid, the local surface density is determined by varying the radial distance as it encompasses the 20th nearest star (for details, refer to Pandey et al. 2020b). In Figure 1, the isodensity contours are shown with the yellow color contours. The lowest contour is at 1σ above the mean stellar density (2.6 stars arcmin^{-2}), while the step size is 1σ (2 stars arcmin^{-2}). The isodensity contours clearly reveal a clustering with two different peaks in the northeast (NE) direction of S301. We refer to this stellar clustering as a NE cluster. This clustering also includes one of the massive stars (ALS 212) whereas the other two massive stars (ALS 207 and ALS 212) are located out of its boundary. The approximate boundary of the NE cluster is shown with a white circle in the Figure 1. The radius of the NE cluster is found to be $3\farcm3$ centered at α_{2000}: $07^{\rm h}10^{\rm m}17\fs51$, δ_{J2000}: $-18^\circ27'35''$.

3.2.2. Membership Probability of Stars in the NE Cluster

The advent of Gaia DR3 data, with its precise measurements of proper motion and parallax, has opened a new horizon in the study of star clusters. We have used the Gaia proper motion (PM) data with $\sigma_{\rm PM} < 3$ mas/yr to determine the membership probability of the stars belonging to the NE cluster found in the S301 region using the method described in Balaguer-Núnez et al. (1998). This method has been extensively used recently

---

[8] https://irsa.ipac.caltech.edu/applications/Gator/
[9] https://gea.esac.esa.int/archive/
[10] https://www.roe.ac.uk/ifa/wfau/halpha/
[11] https://skyview.gsfc.nasa.gov/current/cgi/query.pl
[12] https://skyview.gsfc.nasa.gov/current/cgi/query.pl
[13] https://irsa.ipac.caltech.edu/data/AKARI/
[14] https://www.ipac.caltech.edu/project/planck
[15] https://www.atnf.csiro.au/research/multibeam/release/

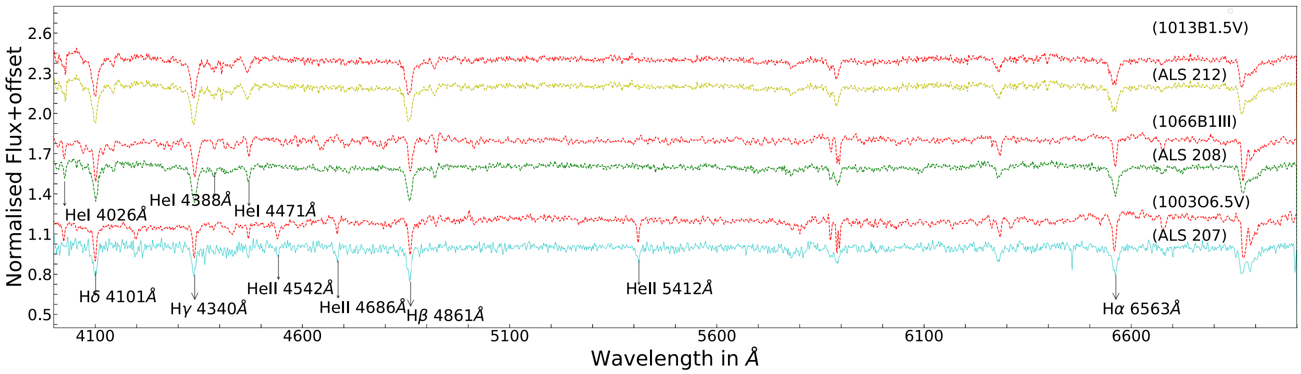

Figure 3. The flux-calibrated and normalized spectra of the sources ALS 207, ALS 208, and ALS 212, shown with cyan, green, and yellow color curves, respectively. For comparison, we have also plotted the standard spectra from the spectral library of Jacoby et al. (1984) in red color. The important spectroscopic lines are also marked in the figure.

(e.g., Kaur et al. 2020; Pandey et al. 2020b; Sharma et al. 2020; Sinha et al. 2020). PMs in R.A. and decl. are plotted as vector-point diagrams (VPDs) in the top panels of Figure 4. The bottom panels show the corresponding V versus $V-I$ color–magnitude diagrams (CMDs). The dots in the top-left panel represent the PM distribution of all the stars in the S301 region ($\sim 18\farcm5 \times 18\farcm5$ FOV), where a prominent clump within a radius of $\sim$0.8 mas yr^{-1} centered at -1.84 mas yr^{-1} ($\mu_\alpha \cos(\delta)$) and 2.74 (μ_δ) mas yr^{-1} can be seen. This population of stars have almost similar PMs and have high probability for cluster membership. Remaining stars with scattered PM values are most probably a field population. This is more clear in the VPDs and CMDs of probable cluster and field populations as shown in the middle and right panels, respectively. The probable cluster members show a well-defined MS in the CMD, which is usually seen for a similar population of stars. On the other hand, the probable field stars are quite obvious by their broad distribution in the CMD. We first construct the frequency distributions of cluster stars (ϕ_c^ν) and field stars (ϕ_f^ν) using Equations (3) and (4) of Balaguer-Núnez et al. (1998). The input parameters such as the PM center and its dispersion for the cluster stars ($\mu_\alpha \cos(\delta) = -1.84$ mas yr^{-1}, $\mu_\delta = 2.74$ mas yr^{-1}, and σ_c, $\sim$0.06 mas yr^{-1}) and field stars ($\mu_{xf} = -0.81$ mas yr^{-1}, $\mu_{yf} = 1.19$ mas yr^{-1}, $\sigma_{xf} = 3.52$ mas yr^{-1}, and $\sigma_{yf} = 3.62$ mas yr^{-1}) are estimated in the same manner as was discussed in our earlier work (Pandey et al. 2020b).

The membership probability (ratio of the distribution of cluster stars with all the stars) for the ith star is then estimated as

$$P_\mu(i) = \frac{n_c \times \phi_c^\nu(i)}{n_c \times \phi_c^\nu(i) + n_f \times \phi_f^\nu(i)}, \tag{9}$$

where n_c (=0.26) and n_f (=0.74) are the normalized numbers of stars for the cluster and field regions ($n_c + n_f = 1$).

We plot the estimated membership probability, errors in the PM, and parallax values as a function of G magnitude in Figure 5. It is clear from the figure that the members are well separated from the field stars in the brighter G magnitude while in the fainter end uncertainty is larger. We have considered only those stars as the members of the NE cluster which have membership probability $P_\mu > 80$ %. Using this criterion, we have identified 194 stars as members of the NE cluster. We further cross-matched 136 of these sources to our optical catalog using a matching radius of 1 arcsecond. The member stars are tabulated in Table 3.

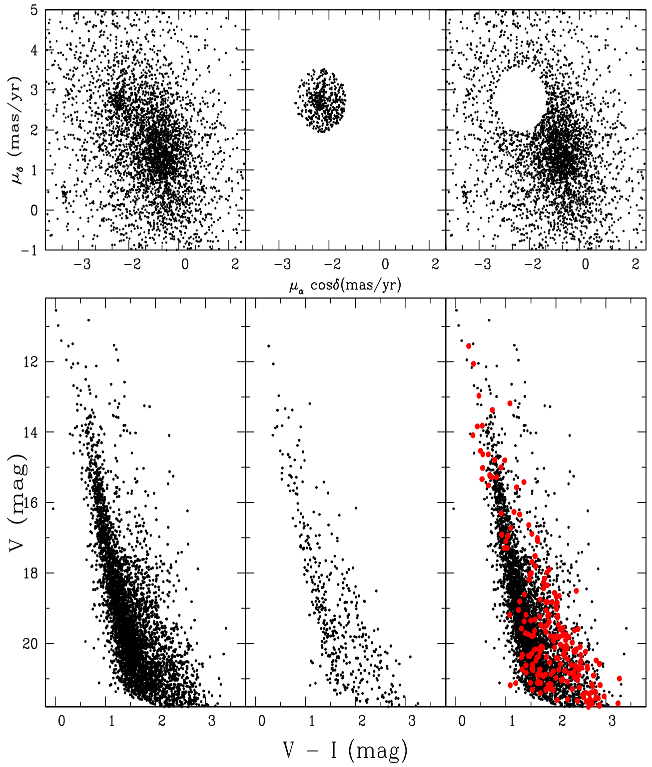

Figure 4. Proper motion vector-point diagrams (top subpanels) and V vs. $(V-I)$ color–magnitude diagrams (bottom subpanels) for the stars located inside the S301 region ($\sim 18\farcm5 \times 18\farcm5$ FOV). The left subpanels show all stars, while the middle and right subpanels show the probable cluster members and field stars, respectively. Red circles in the bottom-right panel are probable member stars of the S301 region.

3.2.3. Reddening, Distance, and Age of the NE Cluster

Two-color diagrams (TCDs) and CMDs of the member stars have been proven to be very good tools to constrain the reddening, distance, and age of a cluster (e.g., Phelps & Janes 1994; Sharma et al. 2006, 2020). In the left panel of Figure 6, we show a $(U-B)$ versus $(B-V)$ TCD of the stars located within the boundary of the NE cluster (radius $<3\farcm3$). The intrinsic zero-age main sequence (ZAMS) from Schmidt-Kaler (1982; blue dotted curve), the member stars (red circles) identified with the Gaia data, and most massive stars are also shown in the figure. We have shifted the ZAMS along the reddening vector, i.e., $E(U-B)/E(B-V) = 0.72$ (corresponding to $R_V \sim 3.1$; see Appendix A), so that it matches with

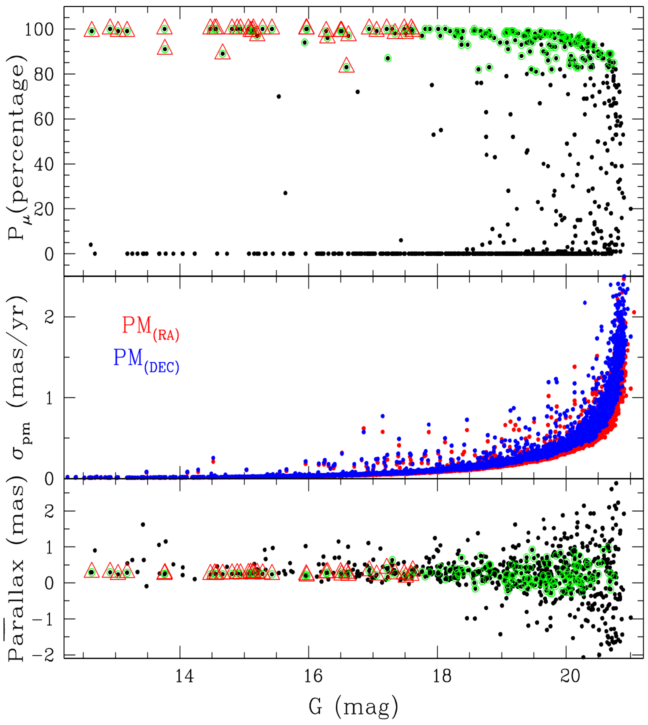

Figure 5. Membership probability P_μ, proper motion errors σ_{PM}, and parallax of stars as a function of G magnitude for stars in the NE-cluster region. The probable member stars ($P_\mu > 80$ %) are shown by green circles while the 37 members of S301 having parallax values with good accuracy (i.e., error <0.1 mas) are shown by red triangles.

the distribution of member stars in the cluster region. The shifted ZAMS is shown with the red continuous curve. By this method, we obtained a foreground reddening value $E(B-V) = 0.50$ mag for the NE-cluster region.

Gaia data releases (DRs) have opened up the possibility of an entirely new perspective on the problem of distance estimation in cluster studies by providing new and precise parallax measurements up to very faint limits.[16] However, the uncertainty of the parallax is such that any parallax that comes with an uncertainty higher that 10% cannot simply be converted into distance in parsecs. Bailer-Jones et al. (2018, 2021) have highlighted that for the vast majority of stars in the Gaia data releases, reliable distances cannot be obtained by inverting the parallaxes. Studies comparing the distances obtained using Gaia DR2 parallaxes with those from other methods show the existence of a systematic offset. The value of the offset ranges from −0.082 to −0.029 mas, depending on the objects and the method used (for details, refer to Arenou et al. 2017; Dias et al. 2021). Recently, Dias et al. (2021) found a systematic offset of -0.05 ± 0.04 mas by comparing the open cluster distances obtained from isochrone fitting with those obtained from a maximum-likelihood estimate of the individual member parallaxes. Using the Gaia data and maximum-likelihood procedure, Cantat-Gaudin et al. (2018) estimated the distance of 1229 open clusters. However, they also highlighted that the distances to clusters with mean parallaxes smaller than ∼0.2 mas would be better constrained by a Bayesian approach using priors based on an assumed density distribution of the Milky Way (Bailer-Jones et al. 2018) or photometric considerations (e.g., Anderson et al. 2018), or simply with more classical isochrone-fitting methods (e.g., Phelps & Janes 1994; Sharma et al. 2006, 2017; Pandey et al. 2020a, 2020b). Therefore, for the present study, we relied on the distance estimates of Bailer-Jones et al. (2021). We have calculated the mean of the distances (Bailer-Jones et al. 2021) of 37 members of the NE cluster having parallax values with good accuracy (i.e., error <0.1 mas, as shown in Figure 5 with red triangles) as 3.54 ± 0.54 kpc. Moffat et al. (1979) calculated the distance of S301 as 5.8 kpc based on spectroscopy of the massive stars ALS 207, ALS 208, and ALS 212. Later on, Avedisova & Palous (1989) estimated the distance of S301 kinematically as 5.1 kpc. With the availability of the Gaia DR3 data, we can now constrain the distances of these stars with better kinematical measurements. The distances of the massive stars ALS 207, ALS 208, and ALS 212 are found to be 3.21 ± 0.14 kpc, 2.99 ± 0.20 kpc, and 2.93 ± 0.19 kpc, respectively (Bailer-Jones et al. 2021). The similar distances of both the NE cluster and massive stars implies that the NE cluster is, in fact, associated with the S301 H II region.

The difference between the spectro-photometric and kinematical distances can be explained by the abnormal reddening law in this region. We have estimated the distances of the massive stars in the region by assuming a normal reddening law, i.e., $R_V = 3.1$ (as assumed by Moffat et al. 1979 and Avedisova & Palous 1989), and an abnormal reddening law, i.e., $R_V = 3.7$. This last is a typical reddening law observed in many Galactic star-forming regions, for example, $R_V = 3.75$ (NGC 6910; Kaur et al. 2020), 3.85 (NGC 7538; Sharma et al. 2017), 3.7 (the Carina region; Kumar et al. 2014), 3.3 (NGC 1931; Pandey et al. 2013), 3.5 (NGC 281; Sharma et al. 2012), and 3.7 (Be 59; Pandey et al. 2008). The individual $E(B-V)$ color excesses of the massive stars ALS 207, ALS 208, and ALS 212 are estimated as 0.80, 0.47, and 0.57 mag (for $R_V = 3.1$) and 0.84, 0.50, and 0.60 mag (for $R_V = 3.7$), respectively, based on the spectral types using the intrinsic color–spectral-type relation given in Schmidt-Kaler (1982). Then, the individual spectro-photometric distances come out to be 5.9, 7.9, and 5.9 kpc (for $R_V = 3.1$) and 4.3, 6.5, and 4.1 kpc (for $R_V = 3.7$) for ALS 207, ALS 208, and ALS 212, respectively, using again the corresponding M_V–spectral-type relation from Schmidt-Kaler (1982). Thus, assuming a normal reddening law can overestimate the spectro-photometric distance, e.g., in the above case, it was overestimated by ∼1.6 kpc and, hence, it can explain the difference between the kinematical (Bailer-Jones et al. 2021) and spectro-photometric (Moffat et al. 1979; Avedisova & Palous 1989) distance estimates. Also, from the above example, it is clear that wrong A_V correction in the case of the abnormal reddening law in the y-axis of the CMD is mostly compensated by the wrong distance estimate, and the change in the individual color excess value for the x-axis of the CMD is minimal, i.e., $E(B-V) \sim 0.035$ mag. Thus, a change in the reddening law might have a marginal effect on the derived physical parameters (for more details, see Sharma et al. 2017).

We plot the CMD for the stars located within the boundary of the NE cluster (radius $<3\overset{\prime}{.}3$) and the member stars in the right panel of Figure 6. The most massive stars in the S301 region are also shown in the figure. The blue continuous curve represents the ZAMS from Pastorelli et al. (2019) corrected for extinction ($E(B-V) = 0.50$ mag) and distance (3.54 kpc). The pre-main-sequence (PMS) isochrones of 0.5 and 5 Myr by Pastorelli et al. (2019) are also shown in the right panel of

---

[16] https://www.cosmos.esa.int/web/gaia/

Table 3
Sample of 137 Stars Identified as Members of the NE Cluster (Having Optical Counterparts)

ID	$\alpha_{(2000)}$ ((deg))	$\delta_{(2000)}$ ((deg))	Parallax $\pm\sigma$ (mas)	$\mu_\alpha \pm \sigma$ (mas/yr)	$\mu_\delta \pm \sigma$ (mas/yr)	G (mag)	$G_{BP} - G_{RP}$ (mag)	Probability (Percentage)	Age $\pm\sigma$ (Myr)	Mass $\pm$ σ ($M_\odot$)	$U \pm \sigma$ (mag)	$B \pm \sigma$ (mag)	$V \pm \sigma$ (mag)	$R \pm \sigma$ (mag)	$I \pm \sigma$ (mag)	$J \pm \sigma$ (mag)	$H \pm \sigma$ (mag)	$K \pm \sigma$ (mag)
1	107.583885	−18.488205	0.103 ± 0.130	−1.691 ± 0.103	2.728 ± 0.108	18.124	2.058	100	1.2 ± 0.32	0.99 ± 0.1	⋯	⋯	18.922 ± 0.090	17.771 ± 0.020	16.940 ± 0.006	15.519 ± 0.011	14.735 ± 0.008	14.466 ± 0.009
2	107.591286	−18.478752	0.265 ± 0.523	−2.020 ± 0.330	3.343 ± 0.496	19.305	2.514	93	0.66 ± 0.08	0.53 ± 0.04	⋯	⋯	19.591 ± 0.031	18.248 ± 0.028	17.181 ± 0.017	15.487 ± 0.009	14.585 ± 0.006	14.275 ± 0.008
3	107.585960	−18.478432	0.709 ± 0.374	−2.003 ± 0.278	2.309 ± 0.302	19.388	2.356	94	1.89 ± 0.47	0.81 ± 0.08	⋯	⋯	19.769 ± 0.021	18.641 ± 0.080	17.652 ± 0.022	16.073 ± 0.033	15.258 ± 0.014	14.928 ± 0.013
4	107.588402	−18.483150	0.337 ± 0.085	−1.758 ± 0.060	2.652 ± 0.073	16.939	1.963	100	0.76 ± 0.26	4.2 ± 0.72	⋯	13.993 ± 0.003	13.186 ± 0.004	12.638 ± 0.008	12.109 ± 0.008	11.214 ± 0.003	10.738 ± 0.003	10.427 ± 0.003

Note. Magnitudes in different bands along with age and mass derived using the color–magnitude diagram analysis are also provided in the table. The complete table is available in electronic form only.

(This table is available in its entirety in machine-readable form.)

Figure 6 with continuous red and black curves, respectively. The shifted ZAMS and PMS isochrones match well with the distribution of member stars, which further confirms the reddening and distance of this cluster. An upper limit to the age of the S301 region can be established from the most massive member star. The location of the most massive star, ALS 207 (O6.5V), in the V versus $(V - I)$ CMD is traced back along the reddening vector to the turn-off point in the main sequence (MS), which is equivalent to a 5 Myr old isochrone (see black curve in Figure 6 right panel). The ages and masses of the member stars of the NE cluster have also been derived by applying the procedure described in our earlier work (Chauhan et al. 2009; Sharma et al. 2017) using the V versus $(V - I)$ CMD. Briefly, we created an error box around each observed data point of a star in the CMD using the errors associated with photometry as well as errors associated with the estimation of reddening and distance. Five hundred random data points were generated by using Monte-Carlo simulations in this box. The age and mass of each generated point were then estimated from the nearest passing isochrone in this CMD. For accuracy, the isochrones and evolutionary tracks were used in a bin size of 0.1 Myr and were interpolated by 2000 points. At the end, we took the mean and standard deviation of age/mass of the above-simulated 500 data points as the final derived values and errors of each star; these are provided in Table 3. The distributions of the estimated age and mass of the member stars are shown in Figure 7, which peak around 1.5 Myr and 0.8 $M_\odot$, respectively. The mean values of the age and mass of the member stars are found to be 3.9 ± 3.2 Myr and 1.3 ± 1.2 $M_\odot$, respectively.

3.2.4. *Mass Function*

The MF is usually expressed by the relation $N(\log m) \propto m^\Gamma$, where the slope of the MF is given by $\Gamma = d \log N(\log m)/d \log m$ and $N(\log m)$ is the number of stars per unit logarithmic mass interval. The MF is generally used as a statistical tool to understand the formation process of stars. It is basically the distribution of a mass of stars formed in a star-forming event. To calculate the MF in the NE cluster of S301, we used the distribution of the masses of the member stars estimated in the previous section. We used only those stars for which the age was less than 5 Myr, i.e., the upper age limit of this region is based on the age of the most massive star. After applying the correction factor for the incompleteness of the photometric data (Section 2.1.1) on the number of stars in different mass bins, we plot the MF in Figure 8. The distribution seems to have no turn-off point. The slope of the MF (Γ) in the mass range $\sim 0.4 < M/M_\odot < 7.0$ comes out to be -0.85 ± 0.07 for the stars in the NE-cluster region.

3.3. *Young Stellar Objects in the S301 Region and their Physical Properties*

The spatial distribution of YSOs and their physical properties can be used to infer the star formation scenario and evolution of a star-forming region. In this study, we have used NIR and MIR observations of the S301 region ($\sim 18\overset{\prime}{.}5 \times 18\overset{\prime}{.}5$ FOV) to identify 37 candidate YSOs based on their excess IR emission. The identification and classification schemes are described in Appendix B. In Table 4, we provide a list of the YSOs along with their magnitudes in different bands and their classification.

We derived the physical properties such as the age and mass of the identified YSOs using spectral energy distribution (SED) fitting analysis. The grid models and fitting tools of Whitney et al. (2003a, 2003b, 2004) and Robitaille et al. (2006, 2007) were used to construct SEDs of the YSOs. This method was used and described in our previous publication (Pandey et al. 2020b). We provided fluxes in optical-to-MIR wavelengths (0.37, 0.44, 0.55, 0.65, 0.80, 1.2, 1.6, 2.2, 3.4, 4.6, 12, and 22 μm) as input data points. Taking extinction and distance as free parameters, the SED fitting tool fits the models to the input data points with a condition that a minimum five data points should be there for fitting. We gave input distances ranging from 3.0 to 4.0 kpc, keeping in mind the error associated with the distance estimation (see Section 3.2.3). The A_V range is given as 1.6 mag (foreground reddening value) to 30 mag (to accommodate deeply embedded YSOs). In Figure 9, a sample SED of a Class II YSO is shown. The black curve represents the best-fit model while the gray curve represents the subsequent well-fit models. The well-fit models for each source are defined by $\chi^2 - \chi^2_{\min} \leqslant 2N_{\rm data}$, where $\chi^2_{\min}$ is the goodness-of-fit parameter for the best-fit model and $N_{\rm data}$ is the number of input

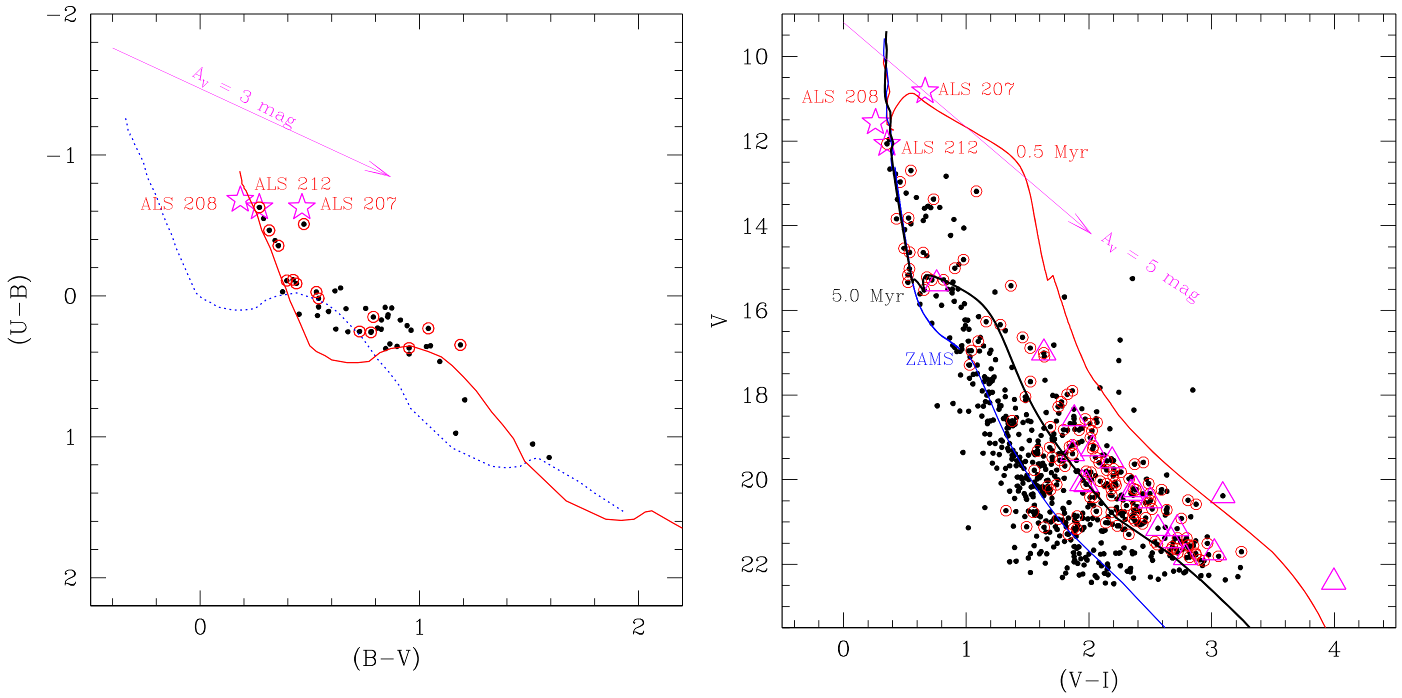

Figure 6. Left panel: $(U-B)$ vs. $(B-V)$ two-color diagram for the sources in the NE-cluster region (radius $<3\overset{\prime}{.}3$, black dots). The identified member stars using proper motion analysis are also plotted with red circles. The dotted blue curve represents the intrinsic zero-age main sequence (ZAMS) for $Z = 0.02$ by Schmidt-Kaler (1982). The red continuous curve represents the ZAMS shifted along the reddening vector (see text for details) by $E(B-V)_{\mathrm{cluster}} = 0.50$ mag for the stars associated with the cluster. Right panel: V vs. $(V-I)$ color–magnitude diagram for the same sources. The ZAMS (blue continuous curve) and pre-main-sequence isochrone for 0.5 and 5 Myr (red and black continuous curves) by Pastorelli et al. (2019), corrected for the distance of 3.54 kpc and reddening $E(B-V) = 0.50$ mag, are also shown. We have also plotted the location of massive stars and young stellar objects (see Section 3.3) by star and triangle symbols in both the figures.

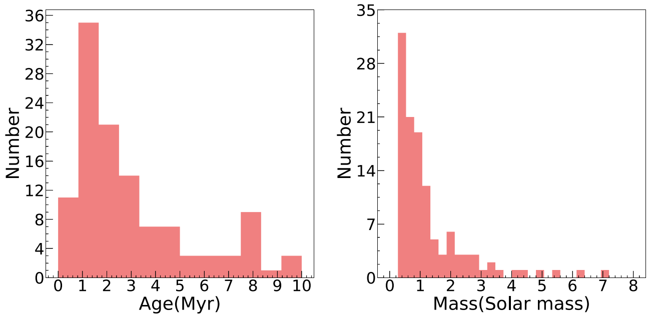

Figure 7. Histograms showing the distribution of the ages (left panel) and masses of the member stars (right panel) of the NE cluster derived using the CMD (Figure 6).

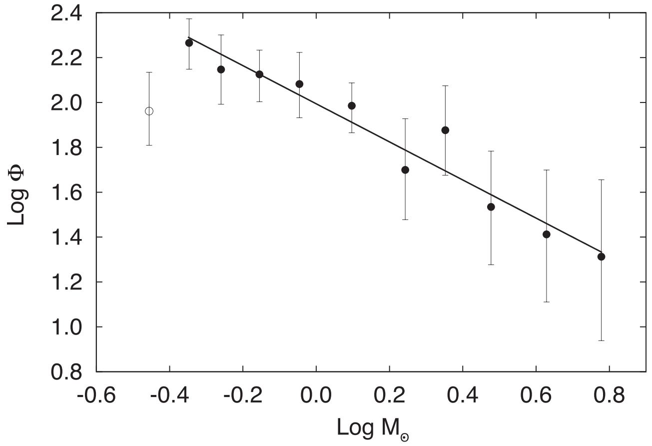

Figure 8. A plot of the mass function (MF) for member stars in the NE cluster. Log ϕ represents $\log(N/\mathrm{dlog}\ m)$. The error bars represent $\pm\sqrt{N}$ errors. The solid line shows the least-squares fit to the MF distribution (black filled circles). The open circle represents the data below the 80% completeness limit.

data points. From the well-fit models for each source derived from the SED fitting tool, we calculated the χ^2 weighted model parameters such as the stellar mass and stellar age of each YSO; they are given in Table 4. Histograms for the age and mass of the YSOs are shown in Figure 10. They peak around 2.5 Myr and 1 $M_\odot$. The mean values of age and mass of the YSOs are found to be 2.5 ± 1.6 Myr and 2.3 ± 0.8 $M_\odot$, respectively. These values are similar to those for the member stars of the NE cluster.

3.4. Distribution of Molecular Cloud Around the S301 Region

In the absence of CO data, we have used the extinction map as a proxy to trace the molecular gas in the S301 region (Gutermuth et al. 2009, 2011; Sharma et al. 2017). We derived the extinction map using the $(H-K)$ colors of the MS stars after removing the sources showing excess IR emission (see Gutermuth et al. 2011). The method is described in Gutermuth et al. (2005, 2009) and has been extensively used recently (Pandey et al. 2020b; Panwar et al. 2020). We have used the NN method to derive the extinction value in a $20'' \times 20''$grid, by taking the mean extinction value of the 20 nearest stars. To obtain the extinction value, we used the relation $E = (H-K)_{\mathrm{obs}} - (H-K)_{\mathrm{int}}$, where $(H-K)_{\mathrm{obs}}$ and $(H-K)_{\mathrm{int}}$ are the observed and intrinsic colors of the MS stars, and then calculated the $A_V = 15.87 \times E(H-K)$ (see Gutermuth et al. 2011). The sources deviating above 3σ were excluded to calculate the final extinction value of each point. Sources showing excess emission in IR can lead to overestimation of the extinction values in the derived maps.

Table 4
A Sample Table Containing Information for 37 YSOs Identified in the S301 Region (18′.5 × 18′.5 FOV)

ID	$\alpha_{(2000)}$ ((deg))	$\delta_{(2000)}$ ((deg))	$U \pm \sigma$ (mag)	$B \pm \sigma$ (mag)	$V \pm \sigma$ (mag)	$R \pm \sigma$ (mag)	$I \pm \sigma$ (mag)	$J \pm \sigma$ (mag)	$H \pm \sigma$ (mag)	$K \pm \sigma$ (mag)	$[3.4] \pm \sigma$ (mag)	$[4.6] \pm \sigma$ (mag)	$[12] \pm \sigma$ (mag)	$[22] \pm \sigma$ (mag)	Class	$N_{\rm data}$	$\chi^2_{\rm min}$	Mass ± σ ($M_\odot$)	Age ± σ (Myr)
1	107.493520	−18.616960	…	…	21.842 ± 0.065	…	19.055 ± 0.014	16.983 ± 0.045	15.990 ± 0.026	15.330 ± 0.026	14.5 ± 0.04	14.116 ± 0.048	9.33 ± 0.102	7.653 ± 0.168	II	9	11.3	2.01 ± 0.89	4.16 ± 3.35
2	107.546871	−18.493279	…	…	21.725 ± 0.078	20.249 ± 0.096	18.703 ± 0.012	15.978 ± 0.013	14.666 ± 0.007	13.773 ± 0.008	…	…	…	…	II	6	0.1	2.54 ± 1.68	1.33 ± 2.21
3	107.596327	−18.488375	…	…	21.441 ± 0.050	…	18.772 ± 0.035	16.859 ± 0.031	15.612 ± 0.014	14.853 ± 0.013	…	…	…	…	II	5	0.1	1.51 ± 1.26	2.26 ± 2.22
4	107.546036	−18.476207	…	…	22.420 ± 0.101	…	18.425 ± 0.009	15.330 ± 0.012	13.800 ± 0.009	12.822 ± 0.009	…	…	…	…	II	…	…	…	…

Note. Magnitudes in different bands along with age and mass derived using the spectral energy distribution analysis are also provided in the table. The complete table is available in electronic form only.

(This table is available in its entirety in machine-readable form.)

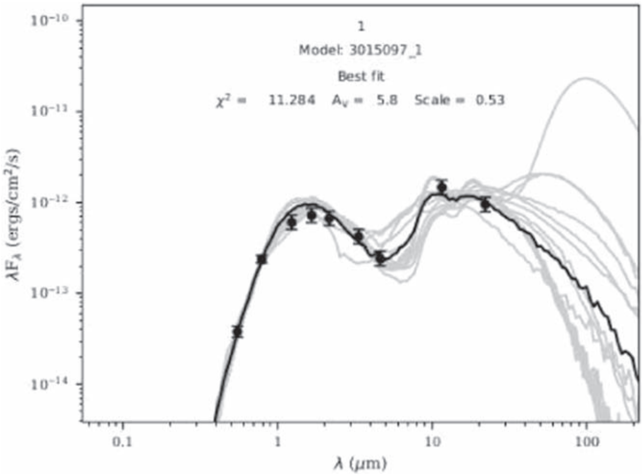

Figure 9. Sample spectral energy distribution (SED) for a Class II YSO created by the SED fitting tools of Robitaille et al. (2007). The black curve shows the best fit and the gray curves show the subsequent well fits. The filled circles with error bars denote the input flux values.

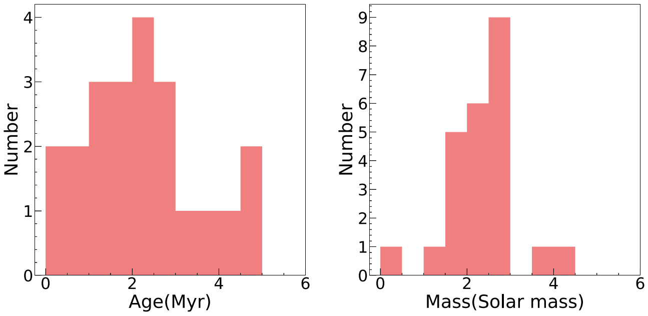

Figure 10. Histograms showing the distribution of the ages (left panel) and masses (right panel) of the YSOs (24) in the S301 as derived from the spectral energy distribution fitting analysis (see Section 3.5).

Therefore, the candidate YSOs and probable contaminating sources are excluded for the calculation of extinction. Here, it is also worthwhile to note that the derived A_V values are the lower limits of their values as the sources with higher extinction may not be detected in our study and the spatial resolution of the map depends on the local stellar density.

3.5. Environmental Conditions of S301

In Figure 11(a), we show a color-composite image of the S301 region made by using WISE 22 μm (red), WISE 12 μm (green), and Hα (blue) images. The figure shows a stunning view of the gas and dust content distributed in the southern and eastern parts of this region. The WISE 12 μm image covers the prominent polycyclic aromatic hydrocarbon (PAH) features at 11.3 μm, indicative of photodissociation regions (or photon-dominated regions, or PDRs). The southern and eastern parts of the complex seem to contain PDRs produced under the influence of massive stars. These features are distributed as arc-like structures, which are probably swept-up gas and dust under the influence of the nearby massive stars. In addition to the above, YSOs are also seen in and around these arc-like structures. The distribution of warm dust at 22 μm near the massive stars shows that the most massive star, ALS 207, has created a warm dust envelope which seems to be bigger in size as compared to that from the less massive star ALS 208. The other massive star, ALS 212, probably lacks a warm dust envelope. The Hα emission seems to trace the full extension of the S301 H II region. Similar structures have been found in several H II regions excited by massive stars (e.g., Deharveng et al. 2010; Paladini et al. 2012). Though the Hα emission is in general spherically distributed, the southeastern peripheries of the S301 region are brighter with few dark lanes whereas the northwestern part has low-intensity extended emission. We notice that the most massive star, ALS 207, is at the center of Hα emission, whereas the other two massive stars are at its boundary.

We have also examined the distribution of colder dust (far-IR, or FIR, emission) in the S301 region using AKARI 160 μm (red), AKARI 60 μm (green), and Hα (blue) images, as shown in Figure 11(b). The cold-dust emission at FIR (traced by 160 and 60 μm) clearly surrounds the hot gas and dust in the south and east directions and is slightly opened up in the northwest direction. Several YSOs are located at the peak of the distribution of cold-dust emission in the northeastern part of this region. This distribution almost mimics the arc-like structures seen at 12 μm, confining the heated region in the south and east directions. The northwestern part of the S301 region is found to be devoid of gas and dust.

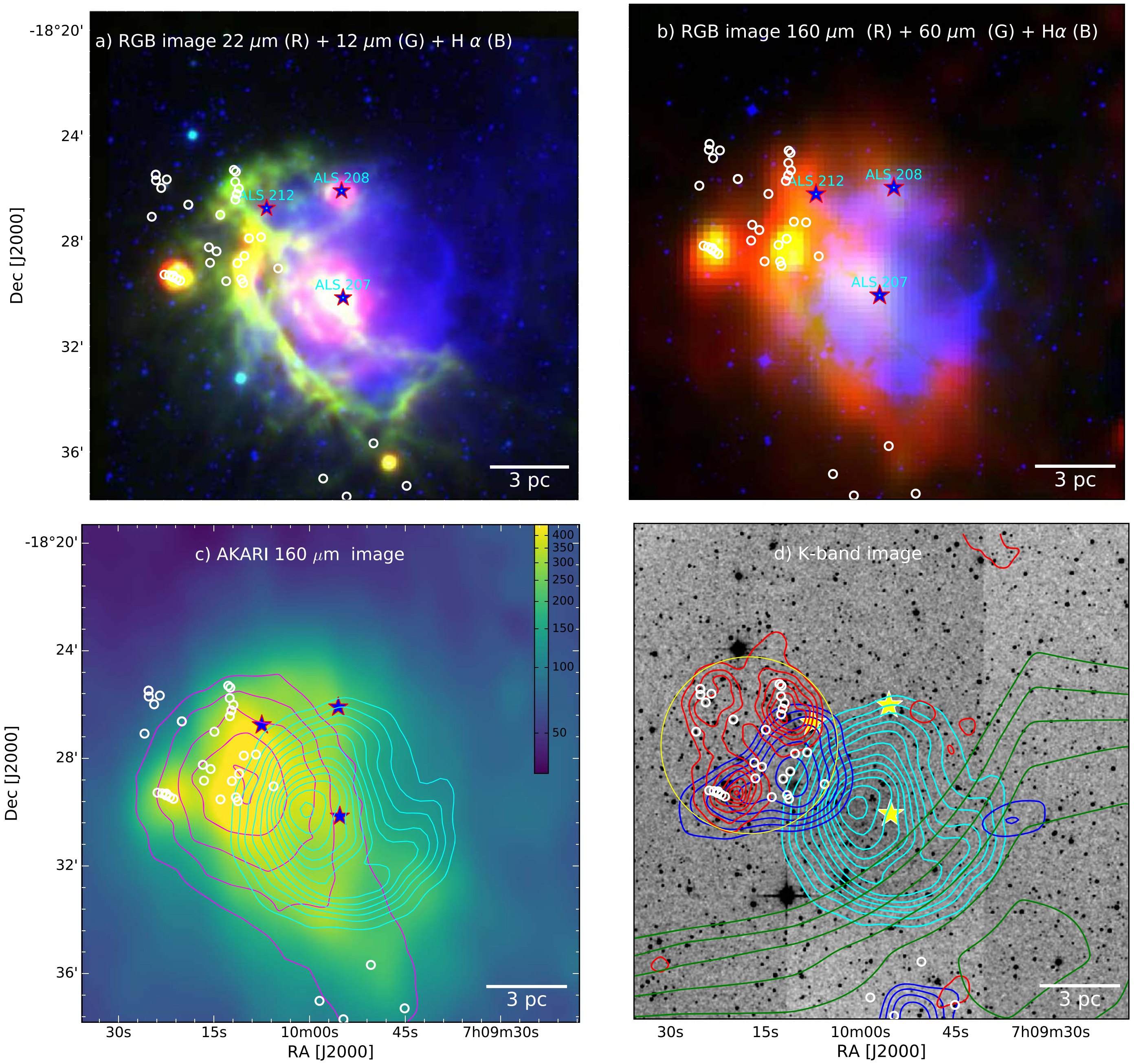

Figure 11. (a) Small-scale view (∼18′.5 × 18′.5) of the S301 shown with a color-composite image made using WISE 22 μm (red), WISE 12 μm (green), and Hα (blue). (b) Color-composite image of S301 created using AKARI 160 μm (red), AKARI 60 μm (green), and Hα (blue) images. (c) The NVSS (cyan) and Planck 870 μm (magenta) contours superimposed on the AKARI 160 μm image. The lowest NVSS contour is at 0.006 Jy/beam and the step size is 0.006 Jy/beam. The lowest Planck contour is at 0.021506 K and the step size is 0.004 K. (d) Cluster surface-density contours (red), extinction-map contours (blue), NVSS radio contours (cyan), and H I map contours (green) superimposed on the 2MASS *K*-band image. The lowest extinction contour is 1σ above the mean value of extinction ($A_V = 4.6$ mag) where the step size is $1\sigma = 0.2$ mag. The lowest H I contour is at 290 K and the step size is 1 K. The cluster surface-density contours are at same level as in Figure 1. The circle and star symbols represent the location of YSOs and massive stars, respectively, in the S301 region.

In Figure 11(c), we also show the NVSS 1.4 GHz radio contours that trace the ionized emission (cyan contours) on the AKARI 160 μm image. Planck 353 MHz emission (magenta contours), which traces cold cloud clumps, is also shown along with the distribution of YSOs and massive stars. Almost all the YSOs are associated with cold gas and dust traced by the AKARI 160 μm and Planck 353 MHz emissions, whereas the massive star ALS 207 is surrounded by ionized gas. The peaks of 160 μm and 353 MHz emission match well with many YSOs located around these peaks. Some of the YSOs are also located at the boundary of the ionized region where the ionized emission seems to be interacting with the cold or warm dust and gas. By looking at the morphology of this region, it appears that the most massive star is at the edge or near the outer surface of the molecular cloud where one can see the embedded YSOs in it.

In Figure 11(d), YSOs along with massive stars are superimposed on the *K*-band image. We also show the radio emission at NVSS 1.4 GHz (cyan contours), extinction contours (blue contours), and stellar surface-density contours (red contours) in the figure. The boundary of the newly identified NE-cluster region (see Section 3.2.1) is shown by a yellow circle. Almost all the YSOs are distributed in the northeastern direction within the boundary of the cluster region with few exceptions in the southern direction. The presence of YSOs inside the cluster region implies that the cluster is very young and thus might have formed via a recent star formation activity. The extinction map shows that most of the molecular material is in front of the cluster at the eastern boundary of the radio emission. The molecular cloud traced by the extinction map is bow-shaped, pointing toward the massive star ALS 207. The peak of radio emission is near to the tip of the bow-shaped molecular cloud, which hints that the radio emission is density bounded in this direction. The distribution of YSOs starts where the ionized emission interacts with the surrounding gas and dust distribution, which could lead us to assume that the formation of YSOs may be due to the interaction of the ionization front with the surrounding material. We have also examined the H I (21 cm) emission in the direction of S301 and found a prominent velocity component ranging from 45 to 60 km^{-1} (see Figure 12). We fitted a Gaussian in the spectrum and found the peak of the velocity component as 52.28 km^{-1}. Fich et al. (1990) and Wouterloot et al. (1988) also reported a radial velocity of ~56.1 km s^{-1} for both the ionized and the molecular gas in the direction of S301. Quireza et al. (2006) have undertaken a radio recombination line survey in this region and reported the line-of-sight radial velocity as ~55.0 km s^{-1} and ~53.7 km s $^{-1}$ for the H and He lines, respectively. These velocities suggest the association of ionized/molecular/neutral gases in the region. In Figure 11(d), we also show the distribution of H I gas integrated over a velocity range of 45 to 60 km^{-1}. The distribution of neutral gas represents the low-density matter in the southwestern part of this region.

3.6. Distribution of the Ionized Gas

In Figure 13(a), we show the distribution of ionized gas using the NVSS 1.4 GHz map, overplotted on the Hα image of the S301 region. The ionized gas is more or less circularly distributed with extended emission in the west direction of the region. The most massive star, ALS 208, is located near the peak of the radio emission whereas the other two massive stars are located at the boundary of the radio emission. The center of the ionized gas is slightly toward the east direction of the region. The observed distributions of the ionized gas, PDR, and cold gas/dust indicate that most of the ionized emission is due to a massive star, ALS 207, and the radio emission is density bounded toward the south and east peripheries. In the other direction, the radio emission is more extended due to the absence of gas and dust material.

Due to the coarse beam size of NVSS ($40'' \times 40''$), small-scale structures are absent in the image and we did not get finer details of the ionized gas distribution. To investigate them, we used the GMRT 1280 MHz emission map (beam size $\sim7'' \times 7''$), overplotted on the Hα image of S301 and as shown in Figure 13(b). The GMRT 1280 MHz emission shows a fragmented dense shell of the ionized gas, which seems to be slightly opened up toward the northwest direction. The ionized gas is density bounded by the PDRs in the southeastern direction, as seen by the 12 μm emission (black contours) in Figure 13(b). The Hα emission also shows similar signatures as discussed in the previous section. It looks like the ionized gas might have streamed out in the lower-density interstellar medium (ISM) through the northwest direction, which has much lesser, or no, gas and dust distribution. We have also estimated the value of the Lyman continuum flux, log($N_{\rm UV}$), as 48.41 (see the next Section 3.7), which corresponds to a O8.5V spectral-type star (see Panagia 1973). Since the main ionizing source, ALS 207, of this H II region has a spectral type of O6.5V (see Section 3.1), the estimated value of the Lyman continuum flux is far less than the expected Lyman continuum flux of an O6.5V star (i.e., log($N_{\rm UV}$) = 49.02). Even if we consider the absorption by dust grains prior to the ionization (Inoue 2001; Binder & Povich 2018), we could not compensate for the remaining value of ionization flux. This also supports our argument that the ionized gas has streamed out from the northwestern direction of this complex. This kind of H II region morphology is already seen in the literature (Tenorio-Tagle 1979; Henney et al. 2005; Krumholz & Matzner 2009; Panwar et al. 2020), where the H II regions open up in the direction away from the cloud edge, and is known as a "blister-type" H II region. This mechanism of flowing ionized gas in the surrounding ISM is known as a "champagne flow" (Duronea et al. 2012; Panwar et al. 2020).

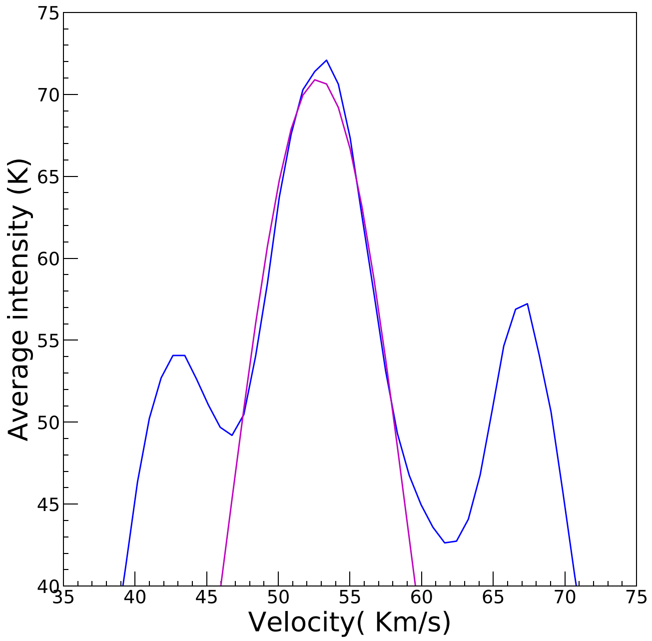

Figure 12. H I (21 cm) spectrum toward the S301 region. A Gaussian (shown with the magenta color) is fitted to determine the peak of the velocity.

3.7. Lyman Continuum Emission and Dynamical Age of the S301 H II Region

We have estimated the Lyman continuum flux associated with the ionized gas in the S301 region by using the following equation by Schmiedeke et al. (2016):

$$N_{\rm UV}(s^{-1}) = 7.5 \times 10^{46}\left(\frac{F_{\rm th}(\nu)}{\rm Jy}\right)\left(\frac{D}{\rm kpc}\right)^{2} \times \left(\frac{T_e}{10^4{\rm K}}\right)^{-0.45} \times \left(\frac{\nu}{\rm GHz}\right)^{0.1}, \qquad (10)$$

where $N_{\rm UV}$ is the Lyman continuum photons per second, T_e is the electron temperature, ν is the frequency, S$_\nu$ is the integrated

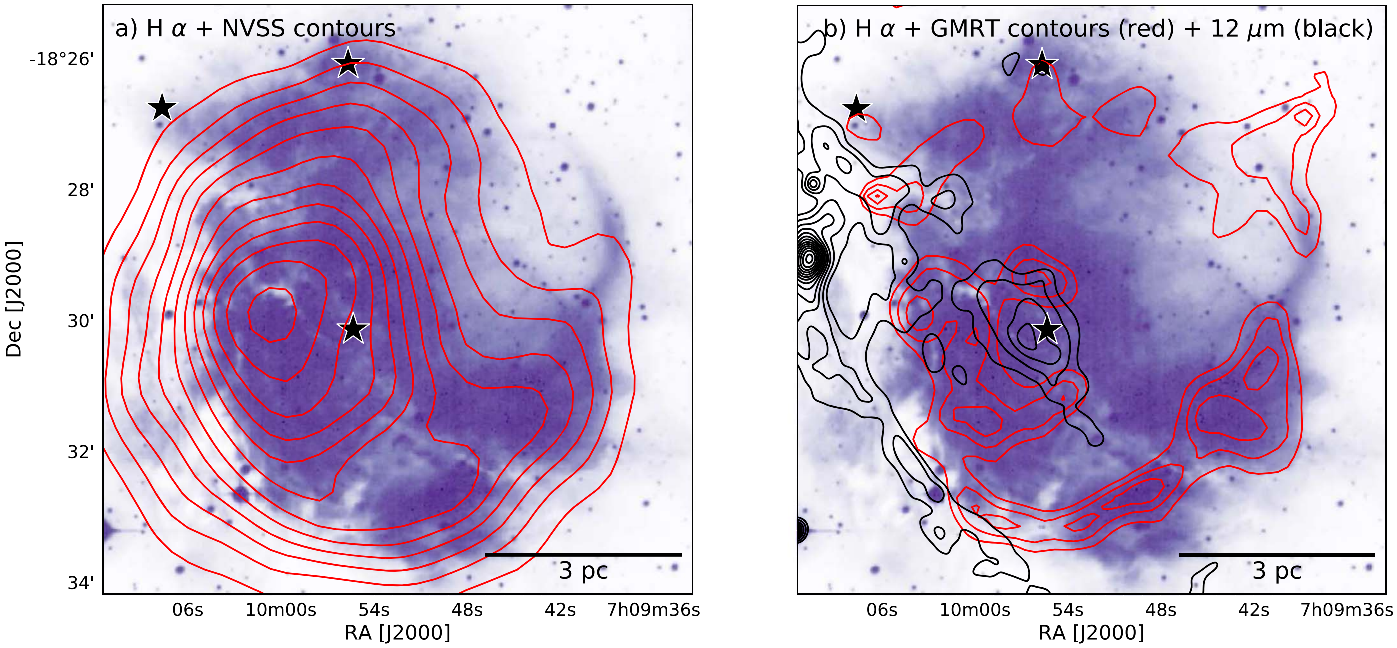

Figure 13. (a) Hα image of the S301 region (FOV $\sim 9' \times 9'$) superimposed with NVSS (1.4 GHz) contours. The lowest NVSS contour is at 0.006 Jy beam^{-1} and the step size is 0.006 Jy beam^{-1}. (b) Hα image of the S301 region superimposed with GMRT (1280 MHz) contours. The lowest GMRT contour is at 0.001 Jy beam^{-1} and the step size is 0.001 Jy beam^{-1}. The star symbols are the locations of massive stars in the region. The beam size of the radio map is shown by a black circle in the lower right corners of the panels. The 12 μm intensity contours are shown with the black color curves, with the lowest contour at 640 counts and the step size of 115 counts.

flux, D is the distance of the region, and θ denotes the angular size of the region. We have adopted values of T_e as 10,000 K, assuming all ionizing flux was generated by a single massive O-type star. We calculated the integrated flux density $S\nu =$ 2.5 mJy by integrating flux down to the lowest contour at the 3σ level in the GMRT 1280 MHz map. The σ value, which is the rms noise of the GMRT radio map, was estimated to be 0.093 mJy/beam. The size of the H II region is found to be $\simeq 4'.7$ (4.8 pc at a distance of 3.54 kpc). Using the distance D of 3.54 kpc, we have estimated the $\log(N_{\rm UV})$ as 48.41.

The dynamical age of the S301 H II region is estimated by using the following equation (Dyson & Williams 1980):

$$t_{\rm dyn} = \left(\frac{4R_s}{7c_s}\right)\left[\left(\frac{R_{\rm H\,\textit{ii}}}{R_s}\right)^{7/4} - 1\right], \tag{11}$$

where c_s is the isothermal sound velocity in the ionized gas ($c_s = 11$ km s^{-1}; Stahler & Palla 2005), $R_{\rm H\,II}$ is the radius of the H II region, and R_s is the Strömgren radius of the H II region, which is given by

$$R_s = \left(\frac{3S_\nu}{4\pi {n_0}^2 \beta_2}\right)^{1/3}, \tag{12}$$

where n_0 is the initial ambient density (in cm^{-3}) and β_2 is the total recombination coefficient to the first excited state of hydrogen, $\beta_2 = 2.6 \times 10^{-13}$ (Stahler & Palla 2005). The dynamical age of the S301 H II region is estimated as 4.8 Myr corresponding to $n_0 = 10^4$ cm^{-3} (Beltrán et al. 2006).

3.8. Feedback Pressure from Massive Star

To quantitatively examine the effect of a massive star on its surroundings, we have determined the feedback pressure from the massive star ALS 207. The total feedback pressure from a massive star consists of three components, the pressure of a H II region ($P_{\rm H\,\textit{II}}$), the radiation pressure ($P_{\rm rad}$), and the stellar wind ram pressure ($P_{\rm wind}$) (Bressert et al. 2012; Dewangan et al. 2017b). These pressure components can be estimated by using the following equations (see, for details, Bressert et al. 2012):

$$P_{\rm H\,\textit{ii}} = \mu m_{\rm H} c_s^2 \left(\sqrt{\frac{3N_{\rm UV}}{4\pi\ \alpha_B\ D_s^3}}\right), \tag{13}$$

$$P_{\rm rad} = L_{\rm bol}/4\pi c D_s^2, \tag{14}$$

$$P_{\rm wind} = \dot{M}_w V_w / 4\pi D_s^2, \tag{15}$$

where $N_{\rm UV}$ is the Lyman continuum photons, c_s is the sound speed in the photoionized region (=11 km s^{-1}; Stahler & Palla 2005), α_B is the radiative recombination coefficient ($=2.6 \times 10^{-13} \times (10^4\ {\rm K}/T_e)^{0.7}$ cm^3 s^{-1}; see Kwan 1997), μ is the mean molecular weight in the ionized gas (=0.678; Bisbas et al. 2009), m_H is the hydrogen atom mass, $\dot{M}_w$ is the mass-loss rate, V_w is the wind velocity of the ionizing source, and $L_{\rm bol}$ is the bolometric luminosity of the ionizing source. We adopted $L_{\rm bol} = 234422\ L_\odot$ (Panagia 1973), $\dot{M}_w \approx 1.21 \times 10^{-7}\ M_\odot$ yr^{-1} (Marcolino et al. 2009), $V_w \approx 5244$ km s^{-1} (Martins & Palacios 2017), and $N_{\rm UV} = 1.047 \times 10^{49}$ (Panagia 1973) for ALS 207 (O6.5V). We took $D_s = 4.24$ pc as the projected distance of the cluster center from the massive star. We gained values of $P_{\rm H\,II} = 8.98 \times 10^{-11}$, $P_{\rm rad} = 1.39 \times 10^{-11}$, and $P_{\rm wind} = 1.86 \times 10^{-12}$ dynes cm^{-2}. The total pressure ($P = P_{\rm H\,II} + P_{\rm rad} + P_{\rm wind}$) comes out to be 1.06×10^{-10} dynes cm^{-2}.

4. Discussion

Broadly, the S301 cloud complex possesses gas and dust, massive stars, an H II region, a young embedded NE cluster, and several YSOs. All of these features hint toward recent star-forming activities in the region. As there are many active star-forming regions in the literature where massive stars have triggered the formation of YSOs (Zavagno et al. 2006; Pomarès et al. 2009; Yadav et al. 2016; Sharma et al. 2017; Kaur et al. 2020; Pandey et al. 2020b, and references therein), in the present work we also explored the impact of massive stars on the star formation activities in the S301 region.

4.1. Feedback from Massive Star

The morphological features discussed in Sections 3.5 and 3.6 point S301 toward a blistered H II region, which is created when a massive star forms at the edge of a molecular cloud. The ionization front soon reaches the edge of the cloud and an H II region opens away from the cloud edge devoid of gas and dust. In the other directions, where the molecular material is distributed, feedback from massive stars can trigger the formation of a new generation of stars. Observational evidence of such triggered star formation have been discussed for several H II regions such as Sh 2-104, RCW 79, Sh 2-212, RCW 120, and Sh 2-217 (Deharveng et al. 2003, 2008; Zavagno et al. 2006, 2010; Brand et al. 2011). Recently, Panwar et al. (2020) studied a blistered H II region, Sh 2-112, and discussed the feedback effect of a massive star in triggering star formation. We have also explored the possibility of triggered star formation in the S301 region. Figures 11 and 13 show the morphology of the S301 star-forming complex. The most massive star, ALS 207, located in the region is responsible for creating the H II region (traced by radio and Hα emission) and arc-like MIR shell/PDRs toward the south and eastern directions of ALS 207. The H I (21 cm) map confirms the presence of low-density neutral hydrogen material at the western border that is devoid of gas and dust. The extinction map shows the presence of molecular clouds in the northeast direction between the NE cluster and the ionization layer of gas. We can also see the presence of YSOs still embedded in the molecular cloud. These facts point to a star formation process triggered by the massive central star ALS 207 in the northeast direction of the S301 region. Earlier, in Section 3.8, we found that the pressure due to the H II region $P_{\mathrm{H\,II}}$ is relatively higher than the other components, i.e., P_{rad} and P_{wind}. Hence, we can argue that the photoionized gas associated with the H II region (against the radiation and wind) can be a major contributor in the feedback process in the S301 region. The total pressure due to the massive star, ALS 207, at the center of the NE cluster was found to be higher than that of a typical cool molecular cloud ($P_{\mathrm{MC}} \sim 10^{-11}$–$10^{-12}$ dynes cm^{-2} for a temperature $\sim$20 K and particle density $\sim 10^3$–10^4 cm^{-3}; see Table 7.3 of Dyson & Williams 1980) and hence can initiate the collapse of the molecular cloud.

Many authors (Pandey et al. 2020b; Kaur et al. 2020) have given age gradient as an argument to support the triggered star formation scenario. To check this, we performed a comparison between the age of the YSOs, the age of the NE cluster, the dynamical age of the H II region, and the age of the massive star. The peaks in the distributions of the ages of the YSOs and NE-cluster members were found to be at $\sim$2.5–1.5 Myr (see Sections 3.2.3 and 3.3). The MF slopes for the cluster region was also found to be shallower ($\Gamma = -0.85 \pm 0.07$) than the Salpeter (1955) value. i.e., $\Gamma = -1.35$. Usually, the higher-mass stars mostly follow the Salpeter MF (Salpeter 1955). At lower masses, the MF is less well constrained, but appears to flatten below 1 $M_\odot$ and exhibits fewer stars of the lowest masses (Kroupa 2002; Chabrier 2003; Lim et al. 2015; Luhman et al. 2016). The MF distribution of the NE cluster indicates that there is a larger population of relatively massive stars, suggesting the youth of this cluster. The dynamical age of the H II region S301 is found to be $\sim$4.8 Myr (see Section 3.7).

Since ALS 207 is of O6.5 spectral type and is still in the MS, hence its age should be $\sim$5 Myr (Meynet et al. 1994; see also Section 3.2.3). The age of ALS 207 is more or less similar to the dynamical age of the H II region S301. Thus, H II region S301 is old enough to initiate the formation of a second generation of stars in its surroundings, which in fact are younger in age. We also calculate the time frame in which the ionization front from the central massive star (ALS 207), with a speed of 9 km s^{-1} (Pismis & Moreno 1976), will reach the NE cluster (4.24 pc) as 1.4 Myr. Hence, we can safely assume that the stars/YSOs in the NE cluster formed after the ionization front from the massive star reached there.

The distribution of the MIR swept-up shell ahead of the layer of ionized gas, along with the NE cluster being on the opposite side embedded in the molecular gas (Figure 11(b)), hint toward a "collect-and-collapse" scenario of star formation in this region (Elmegreen & Lada 1977; Kirsanova et al. 2009; Dewangan et al. 2020b). This scenario predicts a shell of MIR emission around the H II region and the existence of young stellar clusters behind that.

4.2. Formation of Massive Stars: Possibility of a Hub–Filament System

MIR/FIR surveys like Herschel, AKARI, etc., have revealed that the cold ISM, known as the birthplace of stars, is organized in filamentary structures (Men'shchikov et al. 2010; Inutsuka et al. 2015). There have been many studies in which hub–filament systems (HFSs) have been attributed as the possible progenitors of high-mass star formation (Schneider et al. 2012; Dewangan et al. 2017b). Recently, Kumar et al. (2020) have given a detailed explanation regarding the various stages of massive star formation in a HFS. In the HFS, gas flows to the hub via filaments which are the objects of high aspect ratio and low density; the hub is a place where filaments converge and are of low aspect ratio and high density. Initially, flow-driven filaments approach each other due to intra-molecular cloud velocity dispersion, which join to form a hub system. Afterwards, a dense core can form at the junction followed by the formation of massive star(s). These massive stars can further create H II region(s), which can trigger formation of a second generation of stars. In the literature, there are multiple examples of H II regions found in HFSs (Myers 2009; Deharveng et al. 2015; Dewangan et al. 2017a, 2020a).

To explore the possible formation scenario of the massive stars in the S301 region, in Figure 14 we show a large-scale ($0\overset{\circ}{.}7 \times 0\overset{\circ}{.}7$) multiwavelength view of the S301 region. In Figure 14(a), we show a color-composite image made by using the WISE 22 μm (red), WISE 12 μm (green), and optical V-band (blue) images. Figure 14(b) shows a color-composite image made by using the Planck 325 MHz (red), AKARI 160 μm (green), and WISE 22 μm images. It is also superimposed with the NVSS radio and stellar surface-density contours. In both the figures, there is a hint of a central hub of gas and dust along with small filamentary structures (shown with magenta lines). The location of the main ionizing star, ALS 207, at the center of this hub suggests that it may be

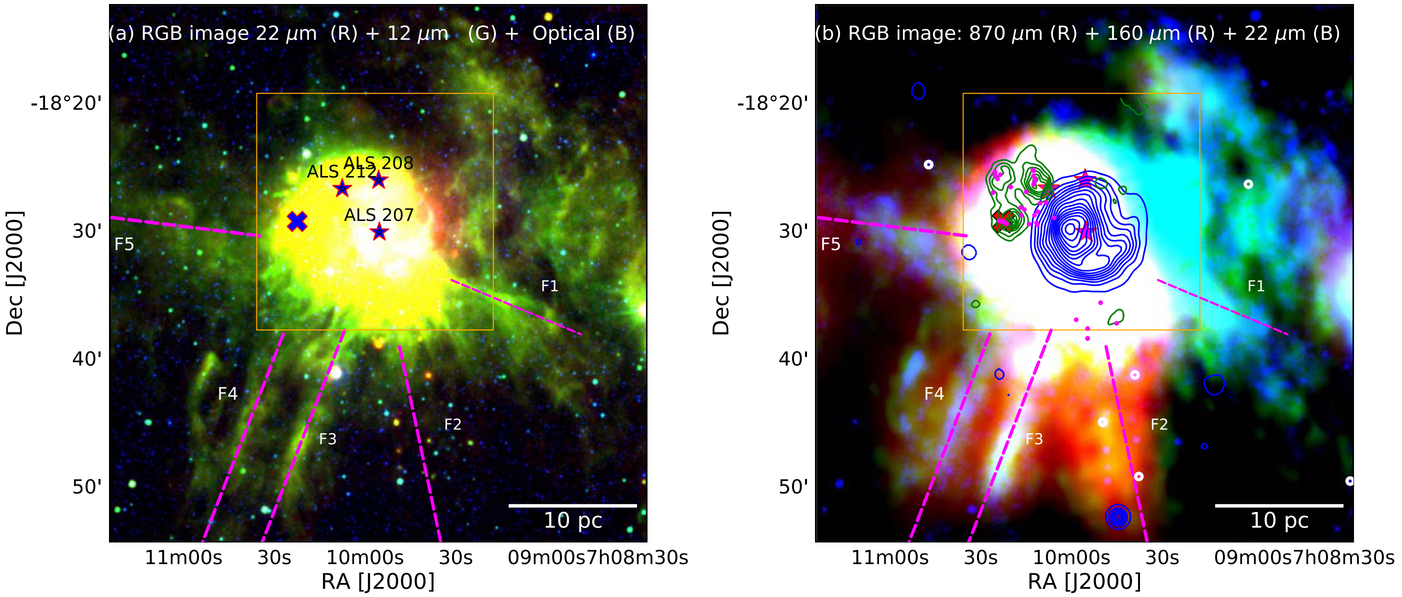

Figure 14. (a) Large-scale view (0°.7 × 0°.7) of the S301 region shown with a color-composite image made by using the WISE 22 μm (red), WISE 12 μm (green), and optical V-band (blue) images. (b) Color-composite image of the S301 region made by using the Planck 353 MHz (red), AKARI (160 μm, green), and WISE 22 μm (blue) images. The NVSS 1.4 GHz contours and stellar surface-density contours are also overplotted over the image in blue and green colors, respectively. The locations of the massive stars and YSOs are also shown by stars symbols and filled circles. The region inside the box is the probable central hub part of the system. Possible filamentary structures are shown by the magenta dashed lines. The cross symbols in both panels show reflection nebula Bran 7D (see Section 1).

formed via HFS-related physical processes. To further confirm the hypothesis of a HFS at S301 being fed by the flow-driven filaments (traced in MIR/FIR wavelengths), we need high-resolution molecular data. Position–velocity (P-V) diagrams along the filaments showing velocity gradient would confirm this hypothesis. Unfortunately, there are no high-resolution data available currently. This will be explored in further studies.

5. Conclusion

We present a multiwavelength study of the H II region S301 using deep optical/NIR data, radio continuum data, and spectroscopic data, along with MIR/FIR archival data taken from different telescopes. From the analyses performed in the present work, we make the following conclusions.

1. Spectral classifications of the massive stars ALS 207 (O6.5V), ALS 208 (B1III), and ALS 212 (B1V) have been done using the optical spectroscopic data taken from the HCT.
2. We have identified a new NE cluster in the northeast direction of the S301 region by doing stellar density-distribution analysis. Gaia DR3 data have been used to identify 194 members of this cluster. We constrained the distance and reddening of this NE cluster as 3.54 kpc and $E(B-V) = 0.5$ mag, respectively. The distance of the NE cluster is similar to that of the H II region S301. Most of the members of the NE cluster have ages and masses around 1.5 Myr and 1.3 $M_\odot$. The slope of the MF Γ in the mass range $0.4 < M/M_\odot < 7$ for the member stars of the NE cluster is found to be -0.85 ± 0.07, which is shallower than the Salpeter (1955) value -1.35.
3. We have identified 37 YSOs in the ~18′.5 × 18′.5 FOV around the massive star ALS 207. The majority of YSOs were found to be spatially associated with the NE cluster. Out of them, four are Class I and the rest are Class II sources. The mean values of the ages and masses of the YSOs is found to be 2.5 ± 1.6 Myr and 2.3 ± 0.8 $M_\odot$, respectively.
4. The morphology of the S301 H II region has been analyzed using the Hα, MIR to FIR, and radio continuum images. The S301 region shows a distribution of hot ionized gas near the massive star ALS 207, which is bounded by an arc-like structure of gas and dust from the southeastern direction. We have found dense molecular material between the massive star ALS 207 and the NE cluster using an extinction map. The northwestern region seems to be devoid of gas and dust material. The distributions of MIR dust, ionized gas, and neutral hydrogen suggest a blister morphology for S301, with the massive star ALS 207 being near the edge of the cloud and the NE cluster being embedded in the cold molecular cloud.
5. The pressure calculation, distribution of PDRs/YSOs, and the age difference between the massive star and the NE cluster provide supporting arguments for the positive feedback of a massive star ALS 207 in the S301 H II region. Our analyses also suggest that the massive stars in the S301 region might have formed in a HFS.

We thank the anonymous referee for several constructive, useful comments and suggestions, which greatly enhanced the quality of the paper. The observations reported in this paper were obtained by using the 1.3 m telescope, Nainital, India, the 2 m HCT at IAO, Hanle, the High Altitude Station of the Indian Institute of Astrophysics, Bangalore, India, and GMRT, Pune, India. We thank the staff of the GMRT that made these observations possible. GMRT is run by the National Centre for Radio Astrophysics of the Tata Institute of Fundamental Research. We acknowledge the TIFR Near Infrared Spectrometer and Imager mounted on the 2 m HCT, using which we have made NIR observations. This publication makes use of

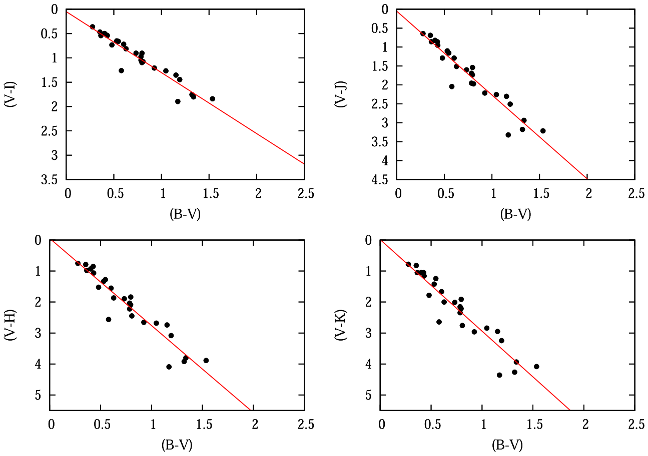

Figure 15. $(V-I_c)$, $(V-J)$, $(V-H)$, $(V-K)$ vs. $(B-V)$ two-color diagrams for the member stars associated with the S301 region. Straight lines show the least-squares fit to the distribution of stars.

data from the 2MASS, which is a joint project of the University of Massachusetts and the Infrared Processing and Analysis Center/California Institute of Technology, funded by the National Aeronautics and Space Administration and the National Science Foundation. This publication makes use of data products from the WISE, which is a joint project of the University of California, Los Angeles, and the Jet Propulsion Laboratory/California Institute of Technology, funded by the National Aeronautics and Space Administration. This publication makes use of data from "HIPASS" survey, carried out by Australia Telescope National Facility's Parkes telescope. The Parkes telescope is part of the Australia Telescope which is funded by the Commonwealth of Australia for operation as a National Facility managed by CSIRO. D.K.O. acknowledges the support of the Department of Atomic Energy, Government of India, under project identification No. Q10 RTI 4002.

Appendix A
Reddening Law

To study the nature of the diffuse ISM associated with the S301 region, we used TCDs to derive the ratio of total-to-selective extinction, $R_V = A_V/E(B-V)$ (Pandey et al. 2003). Although we attained a normal reddening law, $R_V = 3.1 \pm 0.2$ (Guetter & Vrba 1989; Whittet 2003; Lim et al. 2011) in the solar neighborhood, some anomalies have been found in the case of a few star-forming regions (see, e.g., Pandey et al. 2000, 2008; Hur et al. 2012; Pandey et al. 2013; Kumar et al. 2014). The $(V-\lambda)$ versus $(B-V)$ TCDs, where λ represents the wavelengths from one of the broadband filters (R, I, J, H, K, L), are shown in Figure 15. We used all member stars of S301 detected in optical and near-infrared bands, except YSOs (source of contamination due to excess in IR) to generate the TCDs. The method has been discussed in the Appendix of Pandey et al. (2020b). The slopes of the the $(V-I_c)$, $(V-J)$, $(V-H)$, and $(V-K)$ versus $(B-V)$ TCDs, fitted using a least-squares fit, are found to be 1.27 ± 0.15, 2.19 ± 0.17, 2.78 ± 0.19, and 2.92 ± 0.21, respectively. These values are higher than those found for the general ISM (1.10, 1.96, 2.42, and 2.60; see Pandey et al. 2003) by a factor of ~1.1, but considering the errors in the fitting values, we have assumed a normal reddening law ($R_V = 3.1$) for the S301 region.

Appendix B
Young Stellar Object Identification and Classification

To make a census of YSOs in the present study, we used the observed NIR and archival MIR data of S301 in a $\sim 18\overset{\prime}{.}5 \times 18\overset{\prime}{.}5$ FOV around the central massive star ALS 207. We used the following schemes to identify and classify YSOs in the present study. We took the MIR data of S301 from the ALLWISE catalog of WISE, and used the procedure outlined in Koenig & Leisawitz (2014) to identify YSOs. The procedure contains several photometric quality criteria for different WISE bands as well as other selection criteria to isolate candidates like extra galactic contaminants like active galactic nuclei, asymptotic giant branch stars and star-forming galaxies from the sample. In Figure 16 (left panel), we show ([3.4]–[4.6]) versus ([4.6]–[12]) TCD for all the sources belonging to this region. Using this procedure, we identified a single Class I and five Class II sources, shown with blue and green colors, respectively, in Figure 16 (left panel). We also used the observed NIR data from the TIFR Near Infrared Spectrometer and Imager (TIRSPEC) along with the 2MASS data to identify YSOs in the region. For this, we made a combined catalog using the observed NIR data and 2MASS data as the brighter sources are saturated in the TIRSPEC observation and were replaced with the 2MASS data. We also removed those sources from the catalog which have their counterparts in the ALLWISE catalog to cancel out any possible redundancy in YSO identification. The NIR TCD has been used to identify YSOs using the final NIR catalog, and the scheme is well described in Ojha et al. (2004). The NIR TCD is plotted in Figure 16 (right panel) with all the stars in our final NIR catalog. One can see the thick broken curves representing the MS and giant branches (Bessell & Brett 1988); the locus of unreddened Classical T Tauri stars (CTTS; Meyer et al. 1997) is shown by a dotted line. The parallel dashed lines drawn from the tip of the giant branch, the base of the MS branch, and the tip of the intrinsic CTTS line, are the reddening vectors. The sources belonging to the "F" region in the figure are recognized as either field stars or Class III sources, while the sources in the "T" region (between the middle and lower reddening lines) are categorized as the CTTS or Class II sources. The sources falling in the "P" region are classified as Class I sources. Using the NIR data, we finally identified five Class I and 26 Class II sources marked with blue and green colors, respectively, in Figure 16 (right panel). In total, 37 YSOs were identified in the $18\overset{\prime}{.}5 \times 18\overset{\prime}{.}5$ FOV around the central massive star ALS 207.

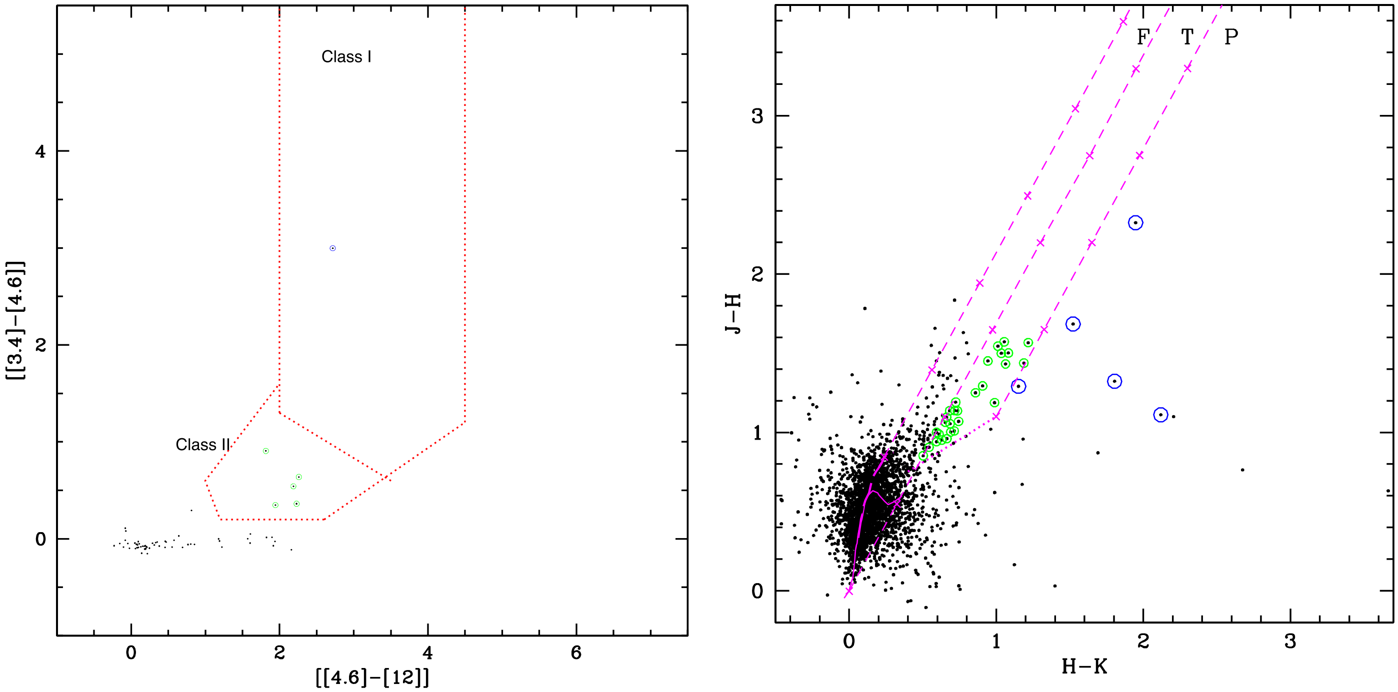

Figure 16. Left panel: ([4.6]–[12]) vs. ([3.4]–[4.6]) two-color diagram (TCD) for the sources in the ∼18′.5 × 18′.5 FOV of S301. The young stellar objects (YSOs) classified as Class I and Class II are based on the color criteria by Koenig & Leisawitz (2014). Right panel: [$H-K$] vs. [$J-H$] TCD (Ojha et al. 2004) for the sources in the same FOV. The continuous and thick magenta dashed curves represent the reddened main sequence (MS) and giant branches (Bessell & Brett 1988), respectively. The dotted magenta line indicates the locus of dereddened Classical T Tauri stars (CTTSs; Meyer et al. 1997). The parallel magenta dashed lines are the reddening lines drawn from the tip (spectral type M4) of the giant branch (left reddening line), from the base (spectral type A0) of the MS branch (middle reddening line), and from the tip of the intrinsic CTTS line (right reddening line). The crosses on the reddening lines show an increment of $A_V = 5$ mag. The YSOs classified as Class I and Class II are shown with blue and green circles, respectively.

ORCID iDs

Rakesh Pandey https://orcid.org/0000-0002-7485-8283
Saurabh Sharma https://orcid.org/0000-0001-5731-3057
Lokesh K. Dewangan https://orcid.org/0000-0001-6725-0483
Devendra K. Ojha https://orcid.org/0000-0001-9312-3816
Neelam Panwar https://orcid.org/0000-0002-0151-2361
Swagat Das https://orcid.org/0000-0002-3658-0516
Arpan Ghosh https://orcid.org/0000-0001-7650-1870
Tirthendu Sinha https://orcid.org/0000-0001-5508-6575

References

Allen, L., Megeath, S. T., Gutermuth, R., et al. 2007, Protostars and Planets V (Tuscon, AZ: Univ. Arizona Press), 361
Anderson, L., Hogg, D. W., Leistedt, B., Price-Whelan, A. M., & Bovy, J. 2018, AJ, 156, 145
Arenou, F., Luri, X., Babusiaux, C., et al. 2017, A&A, 599, A50
Avedisova, V. S., & Palous, J. 1989, BAICz, 40, 42
Bailer-Jones, C. A. L., Rybizki, J., Fouesneau, M., Demleitner, M., & Andrae, R. 2021, AJ, 161, 147
Bailer-Jones, C. A. L., Rybizki, J., Fouesneau, M., Mantelet, G., & Andrae, R. 2018, AJ, 156, 58
Balaguer-Núnez, L., Tian, K. P., & Zhao, J. L. 1998, A&AS, 133, 387
Beltrán, M. T., Brand, J., Cesaroni, R., et al. 2006, A&A, 447, 221
Bessell, M. S., & Brett, J. M. 1988, PASP, 100, 1134
Binder, B. A., & Povich, M. S. 2018, ApJ, 864, 136
Bisbas, T. G., Wünsch, R., Whitworth, A. P., & Hubber, D. A. 2009, A&A, 497, 649
Brand, J., Massi, F., Zavagno, A., Deharveng, L., & Lefloch, B. 2011, A&A, 527, A62
Bressert, E., Ginsburg, A., Bally, J., et al. 2012, ApJL, 758, L28
Cantat-Gaudin, T., Jordi, C., Vallenari, A., et al. 2018, A&A, 618, A93
Chabrier, G. 2003, PASP, 115, 763
Chauhan, N., Pandey, A. K., Ogura, K., et al. 2009, MNRAS, 396, 964
Cutri, R. M., Skrutskie, M. F., van Dyk, S., et al. 2003, VizieR On-line Data Catalog: II/246
Dale, J. E., Haworth, T. J., & Bressert, E. 2015, MNRAS, 450, 1199
Deharveng, L., Lefloch, B., Kurtz, S., et al. 2008, A&A, 482, 585
Deharveng, L., Lefloch, B., Zavagno, A., et al. 2003, A&A, 408, L25
Deharveng, L., Schuller, F., Anderson, L. D., et al. 2010, A&A, 523, A6
Deharveng, L., Zavagno, A., Samal, M. R., et al. 2015, A&A, 582, A1
Dewangan, L. K., Ojha, D. K., & Baug, T. 2017a, ApJ, 844, 15
Dewangan, L. K., Ojha, D. K., Sharma, S., et al. 2020a, ApJ, 903, 13
Dewangan, L. K., Ojha, D. K., & Zinchenko, I. 2017b, ApJ, 851, 140
Dewangan, L. K., Sharma, S., Pandey, R., et al. 2020b, ApJ, 898, 172
Dias, W. S., Monteiro, H., Moitinho, A., et al. 2021, MNRAS, 504, 356
Duronea, N. U., Vasquez, J., Cappa, C. E., Corti, M., & Arnal, E. M. 2012, A&A, 537, A149
Dyson, J. E., & Williams, D. A. 1980, Physics of the Interstellar Medium (Manchester: Manchester Univ. Press)
Elmegreen, B. G., & Lada, C. J. 1977, ApJ, 214, 725
Fich, M., Treffers, R. R., & Dahl, G. P. 1990, AJ, 99, 622
Gaia Collaboration, Brown, A. G. A., Vallenari, A., et al. 2018, A&A, 616, A1
Gaia Collaboration, Prusti, T., de Bruijne, J. H. J., et al. 2016, A&A, 595, A1
Garmany, C. D., Glaspey, J. W., Bragança, G. A., et al. 2015, AJ, 150, 41
Grasha, K., Calzetti, D., Bittle, L., et al. 2018, MNRAS, 481, 1016
Grasha, K., Elmegreen, B. G., Calzetti, D., et al. 2017, ApJ, 842, 25
Guetter, H. H., & Vrba, F. J. 1989, AJ, 98, 611
Gutermuth, R. A., Megeath, S. T., Myers, P. C., et al. 2009, ApJS, 184, 18
Gutermuth, R. A., Megeath, S. T., Pipher, J. L., et al. 2005, ApJ, 632, 397
Gutermuth, R. A., Pipher, J. L., Megeath, S. T., et al. 2011, ApJ, 739, 84
Henney, W. J., Arthur, S. J., & García-Díaz, M. T. 2005, ApJ, 627, 813
Hur, H., Sung, H., & Bessell, M. S. 2012, AJ, 143, 41
Inoue, A. K. 2001, AJ, 122, 1788
Inutsuka, S.-i., Inoue, T., Iwasaki, K., & Hosokawa, T. 2015, A&A, 580, A49
Jacoby, G. H., Hunter, D. H., & Christian, C. A. 1984, ApJS, 56, 257
Jose, J., Pandey, A. K., Ogura, K., et al. 2012, MNRAS, 424, 2486
Kaur, H., Sharma, S., Dewangan, L. K., et al. 2020, ApJ, 896, 29
Kendrew, S., Simpson, R., Bressert, E., et al. 2012, ApJ, 755, 71
Kirsanova, M. S., Wiebe, D. S., & Sobolev, A. M. 2009, ARep, 53, 611
Koenig, X. P., & Leisawitz, D. T. 2014, ApJ, 791, 131
Kroupa, P. 2002, Sci, 295, 82
Krumholz, M. R., & Matzner, C. D. 2009, ApJ, 703, 1352

Kumar, B., Sharma, S., Manfroid, J., et al. 2014, A&A, 567, A109
Kumar, M. S. N., Palmeirim, P., Arzoumanian, D., & Inutsuka, S. I. 2020, A&A, 642, A87
Kwan, J. 1997, ApJ, 489, 284
Lada, C. J., & Lada, E. A. 2003, ARA&A, 41, 57
Landolt, A. U. 1992, AJ, 104, 340
Lim, B., Sung, H., Hur, H., & Park, B.-G. 2015, IAUGA, 29, 2246322
Lim, B., Sung, H. S., Karimov, R., & Ibrahimov, M. 2011, JKAS, 44, 39
Lopez, L. A., Krumholz, M. R., Bolatto, A. D., et al. 2014, ApJ, 795, 121
Luhman, K. L., Esplin, T. L., & Loutrel, N. P. 2016, ApJ, 827, 52
Maíz Apellániz, J., Sota, A., Arias, J. I., et al. 2016, ApJS, 224, 4
Marcolino, W. L. F., Bouret, J.-C., Martins, F., et al. 2009, A&A, 498, 837
Martins, F., & Palacios, A. 2017, A&A, 598, A56
Men'shchikov, A., André, P., Didelon, P., et al. 2010, A&A, 518, L103
Meyer, M. R., Calvet, N., & Hillenbrand, L. A. 1997, AJ, 114, 288
Meynet, G., Maeder, A., Schaller, G., Schaerer, D., & Charbonnel, C. 1994, A&AS, 103, 97
Moffat, A. F. J., Fitzgerald, M. P., & Jackson, P. D. 1979, A&AS, 38, 197
Myers, P. C. 2009, ApJ, 700, 1609
Ninan, J. P., Ojha, D. K., Ghosh, S. K., et al. 2014, JAI, 3, 1450006
Ojha, D. K., Tamura, M., Nakajima, Y., et al. 2004, ApJ, 608, 797
Paladini, R., Umana, G., Veneziani, M., et al. 2012, ApJ, 760, 149
Panagia, N. 1973, AJ, 78, 929
Pandey, A. K., Eswaraiah, C., Sharma, S., et al. 2013, ApJ, 764, 172
Pandey, A. K., Ogura, K., & Sekiguchi, K. 2000, PASJ, 52, 847
Pandey, A. K., Sharma, S., Kobayashi, N., Sarugaku, Y., & Ogura, K. 2020a, MNRAS, 492, 2446
Pandey, A. K., Sharma, S., Ogura, K., et al. 2008, MNRAS, 383, 1241
Pandey, A. K., Upadhyay, K., Nakada, Y., & Ogura, K. 2003, A&A, 397, 191
Pandey, R., Sharma, S., Panwar, N., et al. 2020b, ApJ, 891, 81
Panwar, N., Sharma, S., Ojha, D. K., et al. 2020, ApJ, 905, 61
Pastorelli, G., Marigo, P., Girardi, L., et al. 2019, MNRAS, 485, 5666
Phelps, R. L., & Janes, K. A. 1994, ApJS, 90, 31
Pismis, P., & Moreno, M. A. 1976, RMxAA, 1, 373
Pomarès, M., Zavagno, A., Deharveng, L., et al. 2009, A&A, 494, 987
Quireza, C., Rood, R. T., Balser, D. S., & Bania, T. M. 2006, ApJS, 165, 338
Robitaille, T. P., Whitney, B. A., Indebetouw, R., & Wood, K. 2007, ApJS, 169, 328
Robitaille, T. P., Whitney, B. A., Indebetouw, R., Wood, K., & Denzmore, P. 2006, ApJS, 167, 256
Russeil, D., Georgelin, Y. M., Georgelin, Y. P., Le Coarer, E., & Marcelin, M. 1995, A&AS, 114, 557
Salpeter, E. E. 1955, ApJ, 121, 161
Schmidt-Kaler, T. 1982, in Landolt-Börnstein: Numerical Data and Functional Relationship in Science and Technology, ed. K. Schaifers, H. H. Voigt, & H. Landolt, Vol. 2b (Berlin: Springer-Verlag), 19
Schmiedeke, A., Schilke, P., Möller, T., et al. 2016, A&A, 588, A143
Schneider, N., Csengeri, T., Hennemann, M., et al. 2012, A&A, 540, L11
Sharma, S., Ghosh, A., Ojha, D. K., et al. 2020, MNRAS, 498, 2309
Sharma, S., Pandey, A. K., Ogura, K., et al. 2006, AJ, 132, 1669
Sharma, S., Pandey, A. K., Ogura, K., et al. 2008, AJ, 135, 1934
Sharma, S., Pandey, A. K., Ojha, D. K., et al. 2017, MNRAS, 467, 2943
Sharma, S., Pandey, A. K., Pandey, J. C., et al. 2012, PASJ, 64, 107
Shima, K., Tasker, E. J., & Habe, A. 2017, MNRAS, 467, 512
Sinha, T., Sharma, S., Pandey, A. K., et al. 2020, MNRAS, 493, 267
Stahler, S. W., & Palla, F. 2005, The Formation of Stars (New York: Wiley-VCH), 865
Stetson, P. B. 1992, in ASP Conf. Ser. 25, Astronomical Data Analysis Software and Systems I, ed. D. M. Worrall, C. Biemesderfer, & J. Barnes (San Francisco, CA: ASP), 297
Tenorio-Tagle, G. 1979, A&A, 71, 59
Thompson, M. A., Urquhart, J. S., Moore, T. J. T., & Morgan, L. K. 2012, MNRAS, 421, 408
Walborn, N. R., & Fitzpatrick, E. L. 1990, PASP, 102, 379
Whitney, B. A., Indebetouw, R., Bjorkman, J. E., & Wood, K. 2004, ApJ, 617, 1177
Whitney, B. A., Wood, K., Bjorkman, J. E., & Cohen, M. 2003a, ApJ, 598, 1079
Whitney, B. A., Wood, K., Bjorkman, J. E., & Wolff, M. J. 2003b, ApJ, 591, 1049
Whittet, D. C. B. (ed.) 2003, Dust in the Galactic Environment (2nd edn.; Bristol: IOP Publishing)
Wouterloot, J. G. A., Brand, J., & Henkel, C. 1988, A&A, 191, 323
Wright, E. L., Eisenhardt, P. R. M., Mainzer, A. K., et al. 2010, AJ, 140, 1868
Yadav, R. K., Pandey, A. K., Sharma, S., et al. 2016, MNRAS, 461, 2502
Zavagno, A., Deharveng, L., Comerón, F., et al. 2006, A&A, 446, 171
Zavagno, A., Russeil, D., Motte, F., et al. 2010, A&A, 518, L81